Redox Biology 81 (2025) 103544

Contents lists available at ScienceDirect

Redox Biology

journal homepage: www.elsevier.com/locate/redox

A multi-omics approach reveals impaired lipid metabolism and oxidative stress in a zebrafish model of Alexander disease

Deianira Bellitto [a,1], Matteo Bozzo [a], Silvia Ravera [b,c], Nadia Bertola [d], Francesca Rosamilia [e], Jessica Milia [f], Paola Barboro [c], Gabriela Coronel Vargas [c], Donatella Di Lisa [g], Laura Pastorino [g], Francesca Lantieri [h], Patrizio Castagnola [a], Erika Iervasi [c], Marco Ponassi [c], Aldo Profumo [c], Kateryna Tkachenko [c], Camillo Rosano [c], Simona Candiani [a,c,*], Tiziana Bachetti [c]

[a] Dipartimento di Scienze della Terra, dell'Ambiente e della Vita, Università di Genova, Genova, Italy
[b] Dipartimento di Medicina Sperimentale, Università di Genova, Genova, Italy
[c] IRCCS Ospedale Policlinico San Martino, Genova, Italy
[d] IRCCS Ospedale Policlinico San Martino, Genova, Unità Patologia Clinica, Italy
[e] Bioinformatica Clinica, Direzione Scientifica, IRCCS Istituto Giannina Gaslini, Genova, Italy
[f] Centro di Ricerca, Sviluppo e Studi Superiori in Sardegna (CRS4), Pula, Italy
[g] Dipartimento di Informatica, Bioingegneria, Robotica e Ingegneria dei Sistemi, Università di Genova, Genova, Italy
[h] Dipartimento di Scienze della Salute, Università di Genova, Genova, Italy

ARTICLE INFO

Keywords:
Neurodegeneration
Proteomics
Transcriptomics
Leukodystrophy
Astrocytes
GFAP

ABSTRACT

Alexander disease (AxD) is a rare leukodystrophy caused by heterozygous mutations in the *GFAP* gene. To date, several *in vitro* and *in vivo* models have been generated in an attempt to unravel the main mechanisms underlying this complex disease. However, none of these models is suitable for investigating the global dysregulation caused by AxD. To address this shortcoming, we have generated a stable transgenic zebrafish line (zAxD) carrying the human GFAP p.R239C mutation, which is associated with severe phenotypes of AxD type I patients. We then performed transcriptomics and proteomics analyses on the whole larvae of our zAxD model, confirming the involvement of several pathways such as the immune system response and inflammation, oxidative stress, extracellular matrix, lipoxidation and lipid metabolism, which were previously reported in more limited omic studies. Interestingly, new pathways emerged as well, including tyrosine and butanoate metabolic processes. Biochemical assays confirmed alterations in cell respiration and lipid metabolism as well as elevated oxidative stress. These findings confirm the reliability of the zAxD model to apply a whole-organism approach to investigate the molecular basis of the disease.

1. Introduction

Alexander Disease (AxD) is a rare degenerative disorder of astrocytes, classified under leukodystrophies. The first case of AxD was documented in 1949 when it was diagnosed in a 15-month-old boy exhibiting psychomotor delay and hydrocephalus [1]. Since then, numerous cases of AxD have been identified, leading to the most recent and accepted classification which divides this disease into Type I and Type II, based on time of onset and clinical symptoms [2]. Type I is characterized by early onset (before 4 years old), seizures, abnormal myelination, and developmental delay, while Type II presents late onset (along lifespan) and hindbrain dysfunction such as ataxia, dysphagia, and dysphonia [3]. Type I AxD is the most severe, with a reported two-fold mortality compared to Type II [2]. AxD is a genetically dominant disease and is caused by mutations in the Glial Fibrillary Acidic Protein (*GFAP*) gene, encoding the GFAP protein, the specific Type III Intermediate Filaments of astrocytes [4]. The disease-causing mutations occur in heterozygosity and in most cases *de novo* [5], although rare cases of inherited mutations have been reported [6]. Like other intermediate filament proteins, the GFAP structure is characterized by a central α-helical rod domain, flanked by head and tail domains. Interestingly, all the mutations causing AxD occur in the rod and tail domain

* Corresponding author. Dipartimento di Scienze della Terra, dell'Ambiente e della Vita, Università di Genova, Genova, Italy.
E-mail address: candiani@unige.it (S. Candiani).
[1] Present address: IRCCS Ospedale Policlinico San Martino, Genova, Italia.

https://doi.org/10.1016/j.redox.2025.103544
Received 20 December 2024; Received in revised form 1 February 2025; Accepted 11 February 2025
Available online 13 February 2025

[5] suggesting a role of these regions in the correct formation and assembly of filaments. Moreover, almost half of the AxD cases are due to mutations affecting either the p.R79 or p.R239 codons [7]. AxD patients, even when sharing the same mutation, exhibit phenotypic variability. The cause of this variability is still under investigation, although the major hypothesis is that it is due to genetic modifiers of the disease [5]. When mutated, GFAP filamentous structure collapses into aggregates containing GFAP itself, both mutated and wild-type, αβ-crystallin, ubiquitin, and some proteasome subunits [8,9]. These aggregates, named Rosenthal fibers (RF), are the main feature of AxD and accumulate into the cytoplasm and processes of astrocytes, finally leading to neurodegeneration likely due to impairment in the neuron-astrocyte crosstalk. The exact mechanism by which *GFAP* mutations cause their pathogenic effect is still not completely understood. One of the proposed explanations is that *GFAP* mutations cause a reduction in the rate of GFAP polymerization with the consequent accumulation of toxic intermediates [10]. Moreover, it has been reported that p.R239C GFAP oligomers have an inhibitory effect on the proteasomal activity [11], thus astrocytes themselves activate a positive loop, leading to an increased expression of GFAP, a condition known as gliosis. In addition, it has been reported that even wild-type GFAP overexpression does exert pathogenetic effects, leading to astrocyte hypertrophy and RF formation, resembling the AxD phenotype [12].

To date, there is no cure for AxD except symptomatic treatments. Several *in vitro* and *in vivo* studies tried to identify some compounds as putative pharmacological treatment acting on GFAP expression and/or GFAP aggregation [13–15], but both have limitations. *In vitro* models lack the complexity arising from the interaction between different cell types in the brain, while *in vivo* mouse models are characterized by long gestation times and are difficult to manipulate. However, transcriptomic or proteomic analyses have recently been performed on cellular models of AxD, on brain tissue from AxD patients [16], and on the brain and immunodepleted cerebrospinal fluid of a transgenic mouse model of AxD [17–19].

In the past decades, *Danio rerio*, a simpler vertebrate model also known as zebrafish, has been largely used to model human pathologies, including tumor and neurodegenerative diseases [20,21]. Zebrafish is a small teleost that offers several advantages compared to other *in vivo* models: it is characterized by a fast life cycle, at around 3 months of age fish are sexually mature and can produce up to 400 eggs for each mating. In addition, the external development and transparency of the eggs allow the embryos to be easily manipulated and the expression of fluorescent reporters to be followed [22]. Moreover, the comparison between the human and zebrafish genomes revealed that 76 % of genes implicated in genome-wide association studies (GWAS) for human disease and 82 % of morbid genes present in the Online Mendelian Inheritance in Man (OMIM) database are present in the zebrafish genome [23]. Zebrafish represents a promising model for AxD; indeed, it has been reported that the intron-exon organization of the *GFAP* gene is highly conserved between zebrafish and mammals and the alignment of the amino acid sequences shows 67 % identity [24]. Moreover, it has been shown that zebrafish Gfap protein maintains the same functional properties as protein belonging to type III intermediate filament [24]. The zebrafish brain shows structural and functional features common with the mammalian brain and presents the same cell types of mammals, such as neurons, radial glia, and other glial cell types and microglia [25]. Interestingly, the zebrafish glia also maintains its radial glia identity and neurogenic ability in adults [26]. Recent papers demonstrated the validity of zebrafish for AxD modeling by transient transgenesis [14,27]. However, mosaic expression is not suitable for several studies due to the variability in integration efficiency and, consequently, GFAP expression levels.

In this work, we generated a stable transgenic zebrafish model of AxD (from now on named zAxD) carrying the human p.R239C mutation and exploited it to investigate the main pathways involved in the pathogenesis of this disease by performing the first whole-animal multi-omics analysis on an *in vivo* model of AxD. Our results pave the way for further investigation into the involvement of metabolic processes in AxD.

2. Materials and methods

2.1. Overview of GFAP-GFP expression plasmids

For this work, as a control line we used the zebrafish transgenic line Tg(gfap:GFP)mi2001 previously described by Bernardos and Raymond [28] and obtained by University of Padoa, Italy. The construct used to obtain this line was formed by the *gfap* regulatory elements containing 3 kb of sequence 5-upstream from the initiation codon of *gfap*, the first 16 bp of exon1 and 4.3 kb of intron 1. This regulatory region has already been established to drive expression specifically within glial cells [28]. To generate the Tg(gfap:hGFAP(R239C)-GFP) line we used the plasmid pTol2-gfap:hGFAP(R239C)-GFP, kindly provided by Prof. Choi (Department of Biomedical Sciences and Neurology, Chonnam National University Medical School in Gwangju, Republic of Korea), containing the human mutant GFAP-coding region cloned downstream to the zebrafish *gfap* regulatory elements described above and in frame with 3xFLAG-GFP epitopes [27]. Such construct was also used to generate the transient transgenic line previously reported by Candiani and coworkers (2020).

2.2. Zebrafish care and breeding

The zebrafish were raised and maintained in a system with recirculating freshwater and standard conditions of pH = 7.5 and temperature T = 28.5 °C, and a 14 h light/10 h dark cycle. Adult zebrafish were fed 3 times per day, alternating granular food and *Artemia* nauplii. Spawning of adult zebrafish was performed according to standard methods.

The wild-type fish (AB strain) used to generate the transgenic line, as well as the reporter line Tg(gfap:GFP)mi2001 were obtained from the zebrafish Facility of the University of Padua, Italy. All zebrafish procedures were carried out according to Italian law (D. L.gs 26/2014) and in conformity to Directive 2010/63/EU. The experiments were approved by the Institutional Ethics Review Body of the University of Genoa and the Italian Ministry of Health (authorization release n◦837/2023-PR).

2.3. Generation of zebrafish transgenic line

We successfully generated stable, non-mosaic mutant transgenic line Tg(gfap:hGFAP(R239C)-GFP) by using the Tol2 transposon system which is known to be active in all vertebrates [29]. For the transgenesis the mMESSAGE mMACHINE Kit (Thermo Fisher Scientific, Monza, Italy, Cat. No. AM1344) was used to synthesize the transposase-capped mRNA, using the linearized pCS-TP plasmid as a template. Briefly, using FemtoTip II capillaries an MP-1 micromanipulator, zebrafish eggs, at the stage of one cell (0–0.5 h post fertilization, hpf), were microinjected with 0.5 nL of a mix solution as follow: 280 ng/μL of a GFAP expression construct, 280 ng/μL Tol2 transposase capped mRNA, and 10 % phenol red (Sigma Aldrich, St. Louis, MO, USA, Cat. No.143-74-8). 50 of the F0 microinjected embryos were raised to adulthood and were outcrossed with the wild-type AB strain. Due to the random segregation of the transgene in the F0 germline, the transgene integration has been evaluated through fluorescence microscopy (following protocol of [30]). Subsequently, the screening involved examining both the intensity of fluorescence, which should be uniform, and the percentage of fluorescent embryos that must adhere to the Mendelian ratio (50 % in the case of heterozygous mutations). Only F2 fish showing homogeneous fluorescence and a Mendelian ratio of fluorescence were utilized in our experiments. All the experiments were performed on the F2 progeny for both transgenic lines.

2.4. Confocal imaging

Pigment-reduced 10-days post fertilization (dpf) larvae of both Tg (gfap:GFP)mi2001 and Tg(gfap:hGFAP(R239C)-GFP) were raised in 0.003 % 1-phenyl-2-thiourea (Sigma Aldrich, St. Louis, MO, USA, Cat. No. 103-85-5) and fixed in 4 % PFA/PBS (Thermo Fisher Scientific, Monza, Italy, Cat. No.30525-89-4) for 3 h at room temperature. After thorough rinsing with PBS, the samples were dissected to remove the eyes and the pharyngeal arches, permeabilized with 0.5 % Triton X-100 (Sigma Aldrich, St. Louis, MO, USA, Cat. No. 9036-19-5) in PBS, and incubated in Hoechst (Thermo Fisher Scientific, Monza, Italy, Cat. No. 62249) for nuclear counterstaining. For imaging, the samples were mounted on a microscope slide using Scotch tape as spacers [31]. Confocal images were acquired with a Nikon AX microscope and raw data were analyzed with Fiji [32]. Then, single images were assembled into a table using Adobe Photoshop CS4.

2.5. Immunofluorescence analysis

Larvae of 10 dpf were collected and fixed in 4 % PFA/PBS (Thermo Fisher Scientific, Monza, Italy, Cat. No.30525-89-4) for 3 h at 4 °C for immunohistochemical analysis. After fixation, samples were washed in PBS, sequentially cryoprotected in 30 % sucrose in PBS at 4 °C overnight and then embedded in Tissue-Tek OCT (Electron Microscopy Sciences; Fort Washington, PA). Transverse cryostat sections (10 μm thick) were preincubated in Blocking Buffer (BB) containing 10 % normal goat serum, 0.1 % Triton X-100, and PBS for 1 h at room temperature. Then, sections were incubated o.n. at 4 °C with the following primary antibodies: polyclonal rabbit anti-GFAP (dilution 1:200, Sigma Aldrich, St. Louis, MO, USA, Cat. No. G-9269), mouse anti-HuC/HuD (dilution 1:100, Invitrogen, Milan, Italy, Cat. No. A24271), and mouse anti-GFP (dilution 1:200, Invitrogen, Milan, Italy, Cat. No. A11120). Sections were washed three times, for 5 min each, in PBS and incubated with secondary antibodies: Alexa-546-tagged anti-rabbit and/or Alexa-568-tagged anti-mouse IgG antibody (Invitrogen, Milan, Italy, Cat. No. A-11035 and Cat. No. A-11004) dilution 1:500 in BB. Controls were performed by omitting primary antibodies. Omission of primary antibodies resulted in no immunofluorescence (data not shown). Sections were washed three times in PBS and incubated with Hoechst (Invitrogen, Milan, Italy, Cat. No.33342) for nuclei staining. Images were taken with a Thunder Imaging System (Leica, Milan, Italy) equipped with a LasX advanced image analysis software, and then processed using ImageJ.

2.6. Whole mount in situ hybridization

We conducted whole-mount RNA in situ hybridization on zebrafish following previously established protocols ([21], Candiani et al., 2011). Briefly, fixed embryos were permeabilized using 10 μg/ml of Proteinase K (Sigma Aldrich, St. Louis, MO, USA, Cat. No.39450-01-6) and pre-incubated for 5 h in Hybridization Mix (containing 50 % Formamide, 5X SSC, 0.01 % Tween-20, 50 μg/ml of heparin, and 500 μg/ml of t-RNA; all of them are Sigma Aldrich, St. Louis, MO, USA, Cat. No. respectively 75-12-7; S6639; 9041-08-1).

Expression patterns of *miR-124* were determined by using Locked Nucleic Acid (LNA)-modified oligonucleotide probes (WM-LNA-ISH). LNA-modified probe labeled with DIG at both 5′ and 3 was purchased from Exiqon (Denmark). The sequence of LNA probe for miR-124 was the following: 5′-GGCATTCACCGCGTGCCTTA-3'. Embryos were exposed to a final concentration of 5 nM of the LNA probe at 60 °C. The following day, embryos underwent extensive washing and were incubated in Blocking Solution (2 % sheep serum, 2 mg/ml of BSA in PBS/0.1 % Tween-20) for 2 h. Then, anti-digoxigenin antibody (anti-digoxigenin-AP Fab fragment, Roche, Switzerland; Cat. No. 11207733910) at a 1:3000 dilution was added. After several washes in PBTw, embryos were stained using a Staining solution containing NBT/BCIP (Roche, Switzerland; Cat. No. 11681451001). Stained embryos were mounted in 80 % glycerol and imaged using an Olympus IX70 microscope.

2.7. RNA isolation and sequencing

Total RNA extraction was carried out using 25 larvae from both lines at the 10-dpf stage using a standard Trizol protocol followed by purification with the RNeasy Mini Kit (Qiagen, Milan, Italy, Cat. No. 74134) as previously reported by Ref. [33]. RNA was then quantified using a NanoDrop ND-1000 spectrophotometer (Thermo Fisher Scientific, Monza, Italy) and its integrity was evaluated by running on a denaturing agarose gel. RNA-Seq and transcriptomic analysis were carried out by the CRS4-NGS Core (Cagliari, Italy). For the library preparation, mRNA was isolated from 0,5 μg of total RNA using poly-T oligo-attached magnetic beads and using two rounds of purification (positive selection) as suggested in the TruSeq Stranded mRNA Reference Guide (Illumina, Milan, Italy). Purified samples were processed using TruSeq Stranded mRNA Library Preparation Kit (Illumina, Milan, Italy, Cat. No.20020595). After AMPure XP beads purification (Beckman, Milan, Italy, Cat. No. A63881), DNA fragments were adenylated in their 3' ends, and then IDT for Illumina-TruSeq RNA UD Indexes adapters (Illumina, Milan, Italy) were ligated. A double clean-up of ligated fragments was carried out before library amplification with a 12-cycle PCR. PCR library products were purified with AMPure XP beads (Beckman, Milan, Italy) and quantified using Tecan Infinite F200Pro plate reader (Tecan Trading AG, Switzerland) and Qubit BR dsDNA reagent (Invitrogen, Milan, Italy, Cat. No. Q32850). Quality check and insert size were evaluated using Agilent DNA 1000 assay (Agilent, Cat. No. 5067-1504) on an Agilent Technologies 2100 bioanalyzer (Agilent, Santa Clara, CA, United States). The indexed individual libraries were pooled to obtain equimolar concentrations for each sample and then were loaded on a Paired End Flow Cell using the cBot System (Illumina, Milan, Italy) and the HiSeq 3000/4000 PE Cluster Kit (Illumina, Milan, Italy, Cat. No. PE-410-1001). At the end of the run, around 100 M of 76 bp paired-end reads per sample were generated on a HiSeq3000 instrument (Illumina, Milan, Italy) using HiSeq 3000/4000 SBS Kit reagents (Illumina, Milan, Italy, Cat. No. FC-410-1002).

Finally, demultiplexed FASTQ files were generated according to the Illumina Pipeline data analysis. FASTQ files were processed to identify zebrafish genes and enable quantitative comparisons between gene expression levels. Briefly, the preprocessing step involved alignment to convert FASTQ files into BAM files, which was performed using the Galaxy platform and the STAR tool [34], following the guidelines provided in the Reference-based RNA-Seq Data Analysis training materials (https://training.galaxyproject.org/training-material/topics/transcriptomics/tutorials/ref-based/tutorial.html). The analysis utilized the zebrafish genome assembly GRCz11 (NCBI RefSeq assembly: GCF_000002035.6). After generating BAM files, HTSeq-count [35] was used to count the number of sequencing reads mapped to each annotated gene. The output of this step was subsequently analyzed in the R environment to perform quantitative comparisons of fold change (FC) between the mutated and control groups (treatment-to-control comparison). For the R-based analysis, the following libraries were employed: GenomicFeatures and GenomicAlignments [36], TxDb.Drerio.UCSC.danRer11.refGene (https://doi.org/10.18129/B9.bioc.TxDb.Drerio.UCSC.danRer11.refGene), BiocParallel [37], edgeR [38], and DESeq2 [35]. Since sequencing was performed only once for each animal batch group, no inferential statistical tests were conducted. As a result of the transcriptomic analysis, a table was produced containing the following information for each gene: Gene Symbol, read count per sequencing group, and fold change (FC) values. Differentially expressed genes were identified using a fold-change threshold of $-1 \leq \log2(FC) \geq 1$, excluding genes with fewer than 5 counts in either group.

RNAseq.raw data are available at the Biosample repository of National Institute of Health with the BioSampleAccession: SAMN38050941 ID: 38050941 (for Tg(gfap:hGFAP(R239C)-GFP line) and BioSampleAccession: SAMN38050940 ID: 38050940 (for Tg(gfap:GFP)

mi2001 line).

2.8. Gene expression analysis by qRT-PCR

RNA template (1 μg) was prepared as reported previously, and reverse transcription reaction was performed with SuperScript IV Kit (Invitrogen, Milan, Italy, Cat. No.18091050) according to the instruction manual. The StepOnePlus Real-Time PCR System (Applied Biosystems, Foster City, CA, USA) was used for RT-qPCR. For qRT-PCR, 10 μl of iQ Supermix (Biorad, California, USA; Cat. No. 1708860), 1 μl of 20 X Gene Expression Assay, 5 μl of cDNA template, and 4 μl of sterile distilled water were used as the reaction solution, for a total of 20 μl per sample dispensed in each well. Taqman Gene Expression Assay was used as the primer for the following genes: Ifit8 (Applied Biosystems, Cat. No. 4448892), Ifi27.1 (Applied Biosystems, Cat. No. 4448892) and beta-actin as housekeeping (Applied Biosystems, Cat. No.4453320). For the reaction conditions, initial activation was performed at 95 °C for 3 min, followed by 40 cycles of thermal denaturation at 95 °C for 10 s, and annealing and elongation at 55 °C for 30 s. All reactions were performed in triplicate and carried out in the MJ Mini Biorad Real Time PCR (Biorad, California, USA). The delta–delta CT method was used to determine the fold change for relative gene expression. Statistical analysis was performed using Prism 8 Software as reported in the paragraph 2.20 (GraphPad Software Inc., Boston, MA, USA).

2.9. Protein isolation

For proteomics analysis, 50 embryos at 10 dpf and 20 dpf for each line were collected. The number of animals was the one sufficient to guarantee at this stage at least 100 μg of protein preparation, necessary for the following MS analysis. Zebrafish embryos were pottered and passed through a 70 μm diameter filter before undergoing a wash with PBS added with protease (20 g/ml leupeptin, 25 g/ml aprotinin, 10 g/ml pepstatin, 0.5 mM benzamide) and phosphatases inhibitor (1 mM Na_3VO_4, Merck, Darmstadt, Germany, Cat. No. 13721-39-6) followed by centrifugation at 4 °C, 1500 rpm for 15 min. The pellet was then lysed by RIPA buffer incubated at 4 °C for 60 min, vortexed every 15 min four times and then sonicated for 30 s with pulse (at approximately 10 W output). Samples were centrifuged at 13,850 rcf for 10 min. Then, supernatants were collected, their volumes were measured, and the same amount of 20 % SDS-6% DTT was added. Subsequently, they were incubated at 95 °C for 5 min. Once cooled, five volumes of MATF (Methanol, Acetone, and Tributhyl phosphate, 1:12:1) were added, and samples were incubated for 1 h with agitation. The total proteins were finally pelleted by centrifugation at 12,000 rcf for 15 min, the supernatants were removed, and the protein precipitates dried for about 30 min at RT in a Savant SpeedVac apparatus (Thermo Fisher Scientific, Waltham, MA, USA). The dried pellets were resuspended in 250 μL of 5 % SDS in 50 mM Ammonium Bicarbonate (AMBIC). Then, using the QuantiPro BCA Assay Kit (Sigma-Aldrich, St. Louis, MO, USA), each sample was processed to determine its protein concentration. Later, 20 mM DTT was added to 50 μg of each total protein extract, and the samples were incubated at 95 °C for 10 min. Then, when cooled to RT, Iodoacetamide was added to a final concentration of 40 mM, and the reaction mixtures were incubated for a further 30 min in the dark. Finally, orthophosphoric acid was added to a final 1.2 % concentration. After reduction and alkylation, the acidified protein samples were loaded onto S-Trap mini columns, washed four times, and successively trypsin-digested as suggested by the manufacturer at 37 °C for 1h and blocked with 50 % acetic acid (Sigma Aldrich, St. Louis, MO, USA, Cat. No. 64-19-7) in a 1:10 ratio. Following agitation for 10 min at RT, proteins have been dried under vacuum and stored at −80 °C until use (Protifi, Farmingdale, NY, USA). The eluted mixtures were dried under vacuum at RT in a Savant SpeedVac apparatus (Thermo Fisher Scientific, Waltham, MA, USA).

2.10. Mass spectrometry

An Ultimate 3000 chromatography system (Thermo Scientific Instruments, Waltham, MA, USA), equipped with a PepMap RSLC C18 EASY spray column (Thermo Scientific, Waltham, MA, USA, Cat. No. 13294749) was used to analyze the tryptic digests at a flow rate of 250 nl/min and a temperature of 60 °C. Eluate was analyzed by mass spectrometry (MS) using a Q Exactive™ Plus Hybrid Quadrupole-Orbitrap™ mass spectrometer equipped with an Easyspray source (both Thermo Scientific Instruments, Waltham, MA, USA). The data were acquired, in the mass range between 200 and 2000 m/z, in data-dependent (DDA) mode alternating between MS and MS/MS scans, using the software Xcalibur (version 4.1, Thermo Scientific Instrument, Waltham, MA, USA). MS scan resolution was 70,000 with an automatic gain control (AGC) target of 3.0E6 and a maximum injection time (maxIT) of 100 ms. MS/MS spectra resolution was 17,500, with an AGC target of 1.0E5 and a maxIT of 50 ms. The precursor isolation window was 2.0 m/z and higher-energy collisional dissociation has been performed using 30 normalized collision energy (NCE).

2.11. Mass spectrometry data analysis

Data from mass spectrometer analysis in *.RAW format was deposited to the ProteomeXchange Consortium via the PRIDE [39] partner repository with the dataset identifier PXD040214 (DOI: 10.6019/PXD040214; Pride: https://www.ebi.ac.uk/pride/archive/, https://www.ncbi.nlm.nih.gov/sra/SRX22318631, https://www.ncbi.nlm.nih.gov/sra/SRX22318630; Bioproject: https://www.ncbi.nlm.nih.gov/bioproject/).

Mass spectrometer data was processed with ProteomeDiscoverer® (v. 2.4.1.15) (Thermo Scientific Instrument, Waltham, MA, USA) using a workflow adapted to LTQ ORBITRAP label-free quantification. Briefly, in the processing step we used *Danio rerio* - tr_canonical v2022-03-02 database for peptide spectral matches identification in MS/MS spectra and concatenated decoy (Target False Discovery Rate strict = 0.01, Target False Discovery Rate relaxed = 0.05 for proteins, peptides and peptide spectral matches). Protein quantification was calculated by peptides summed abundances, and the differential analysis was performed pairwise ratio-based and *t*-test background-based using the IMPapQuant node [40]. After conducting a proteome differential analysis, differentially expressed proteins (DEPs) were identified for each experimental point. These DEPs were then used in a Kolmogorov-Smirnov test to calculate the top 20 most significant Gene Ontology-Biological Process (GO-BP) enrichment annotations. The Kolmogorov-Smirnov test was performed using the topGO package [41] and the org.Dr.eg.db package, both of which are Bioconductor packages in the R environment.

2.12. Gene-set enrichment analysis

Differential expressed transcripts and proteins were analyzed by comparing with both global background with Enrichr (https://maayanlab.cloud/Enrichr/), ShyniGO v0.75 (http://bioinformatics.sdstate.edu/go75/), PANGEA (PAthway, Network and Gene-set Enrichment Analysis) (https://www.flyrnai.org/tools/pangea/web/home/7955).

Gene Ontology Biological Processes (GO-BP) and Molecular Function (GO-MF), in addition to KEGG and Reactome pathways resources were investigated for the 10dpf and 20dpf conditions. The p-value<0,05 cutoff was selected for all the analyses and the graphed terms were only those resulted statistically significant.

In ShyniGO, the color scale from red to blue is inversely related with the fold enrichment; the circles positively correlate with the number of genes. The length of the bar is inversely correlated with the p-value score (-Log10 p-value).

Moreover, the Reduce + visualize Gene Ontology REVIGO web tool [42] (http://revigo.irb.hr/) was used to cluster and visualize the Enrichr

GO-BP groups ranked by p-value<0,05. The size of each GO was determined by a bubble chart in which the quantity of genes in each GO term is represented by the size of the bubble. The color scale from yellow to red indicated the increasing extent of significance. The two-dimensional space is derived by applying multidimensional scaling to a matrix of the GO terms' semantic similarities.

2.13. Zebrafish homogenate preparation

Metabolic analyses were carried out on the homogenate of whole zebrafish at different time points post-fertilization. The homogenate was obtained by borosilicate glass Potter-Elvehjem Homogenizers, resuspending the animals in 0.5 ml of PBS, and the sample protein concentration was evaluated by the Bradford method [43].

2.14. Oxidative phosphorylation metabolism evaluation

Oxygen consumption rate (OCR) and ATP synthesis through F_oF_1 ATP-synthase were evaluated at 10 and 20 dpf as markers of oxidative phosphorylation (OxPhos) metabolism. For each of these analyses, 50 μg total protein of whole zebrafish homogenate was used. OCR was measured with an amperometric electrode (Unisense Microrespiration, Unisense A/S, Aarhus, Denmark) in a closed chamber at 25 °C. 10 mM pyruvate +5 mM malate (P/M; Merck, Darmstadt, Germany Cat. No. P4562 and Cat. No. M8304, respectively) or 20 mM succinate (Succ; Merck, Darmstadt, Germany Cat. No. S7501) were added to stimulate oxygen consumption, to stimulate the pathways composed by respiratory complexes I, III, and IV or II, III and IV, respectively. In both experiments, 0.1 mM ADP (Merck, Darmstadt, Germany Cat. No. A5285) was added after the addition of the respiratory substrates.

ATP synthesis was evaluated using the luciferin/luciferase chemiluminescent method (luciferin/luciferase ATP bioluminescence assay kit CLS II, Roche, Switzerland, Cat. No.11699695001), with a luminometer (GloMax® 20/20 Luminometer, Promega Italia, Italy), for 2 min every 30 sec. 10 mM pyruvate +5 mM malate or 20 mM succinate were employed as respiratory substrates. The reaction was observed after the addition of 0.1 mM ADP.

To evaluate the OxPhos metabolism efficiency, P/O values were calculated as the ratio between the aerobic synthesized ATP and the consumed oxygen, both expressed as nmol/min/mg. Efficient mitochondria display a P/O value of around 2.5 and 1.5 when stimulated with pyruvate and malate or succinate, respectively [44]. A P/O ratio lower than 2.5 or 1.5 indicates that oxygen is not completely devoted to energy production, contributing to reactive oxygen species (ROS) production [45].

2.15. Antioxidant enzyme activities evaluation

Catalase (CAT), Glutathione reductase (GR), and Glutathione peroxidase (GPx) were assayed as markers of cellular antioxidant defenses. For each assay, 50 μg of zebrafish homogenate protein were used. CAT activity was assayed spectrophotometrically following the H_2O_2 decomposition at 240 nm [46]. GR activity was assayed spectrophotometrically at 340 nm, following the NADPH oxidation [46]. GPx activity was evaluated following the H_2O_2 decomposition at 240 nm, in the presence of 5 mM GSH (Merck, Darmstadt, Germany Cat. No. G6529). Since H_2O_2 is also a substrate of catalases, GPx activity is obtained by subtracting the result of this assay from the catalase activity values [47].

2.16. NADPH oxidase activity assay

The enzymatic activity of NADPH oxidase (NADPHox) was assessed following the cytochrome C reduction on 50 μg of zebrafish homogenate total protein. The assay mixture contained: 60 mM cytochrome C (Merck, Darmstadt, Germany Cat. No. C5499), 1 mM $CaCl_2$, and 1 mM $MgCl_2$ with (for the samples) or without (for the blank) 20 mg/ml SOD (Merck, Darmstadt, Germany Cat. No. S9697) in a total volume of 400 μl of phosphate buffer saline (PBS, pH = 7.4). After incubation at 37 °C for 5 min, the samples were centrifuged at 800×*g* for 5 min at 25 °C, and the absorbance was monitored at 550 nm [48].

2.17. Superoxide anion assay

The production of superoxide anion was measured by the mean of the difference between total and SOD-inhibitable cytochrome C reduction on 50 μg of zebrafish homogenate total protein. Samples were incubated in a solution containing: 100 mM Tris-HCl, pH 7.4, 100 μM cytochrome C, and 300 U SOD, if present. After 10 min of incubation at 37 °C, samples were centrifuged at 12,000×*g* for 8 min and reduced cytochrome C was measured in the supernatant by spectrophotometry at 550 nm [49].

2.18. Lipid peroxidation evaluation

Malondialdehyde (MDA) concentration was assessed spectrophotometrically at 532 nm, using the thiobarbituric acid reactive substances (TBARS) assay on 50 μg zebrafish homogenate total protein to evaluate lipid peroxidation damages [50].

2.19. Fatty acid metabolism evaluation

The activity of 3-hydroxyacyl-CoA dehydrogenase and β-ketoacyl-ACP reductase were assayed as markers of fatty acids β-oxidation and synthesis, respectively.

3-hydroxyacyl-CoA dehydrogenase assay was performed spectrophotometrically at 340 nm, following the oxidation of NADH in the presence of acetoacetyl-CoA [50].

β-ketoacyl-ACP reductase was assayed following the oxidation of NADPH in the presence of acetoacetyl-CoA [50].

2.20. Statistical analysis

Biochemical data are expressed as mean ± standard deviation (SD), and errors with a probability of $p < 0.05$ were considered significant. Statistical analyses were performed using the unpaired *t*-test or analysis of variance (one-way ANOVA) followed by Tukey's multiple comparison test, by Prism 8 Software (GraphPad Software Inc., Boston, MA, USA). qRT-PCR data are expressed as mean ± standard deviation (SD) and errors with a probability of $p < 0.05$ were considered significant. The normality of the data was verified by the Shapiro-Wilk test. The presence of outliers was determined by the ROUT test and no data were excluded. Statistical analyses were performed using the unpaired *t*-test for Ifit8 validation, and unpaired *t*-test with Welch's correction for Ifi27.1, by Prism 8 Software (GraphPad Software Inc., Boston, MA, USA).

3. Results

3.1. The R239C mutation causes GFAP aggregation in zebrafish larvae, recapitulating the major feature of the Alexander disease

Our zAxD was created by inserting the human *GFAP* gene with the missense mutation p.R239C, which causes one of the most severe phenotypes of the disease, under the transcriptional control of the zebrafish *gfap* promoter. To validate the model, we assessed the presence of fluorescent aggregates in F2 larvae of the Tg(gfap:hGFAP(R239C)-GFP) line. The p.R239C-GFP aggregates were clearly visible throughout the central nervous system of zAxD larvae at 20 dpf and particularly abundant at the level of the telencephalon and cerebellum (Fig. 1d–f). Some brain regions of the zAxD also contained GFAP with an elongated pattern as shown by the Tg(gfap:GFP)mi2001 control line (Fig. 1f and a-c). The structure of plasmids utilized for transgenic lines is illustrated in Fig. 1g.

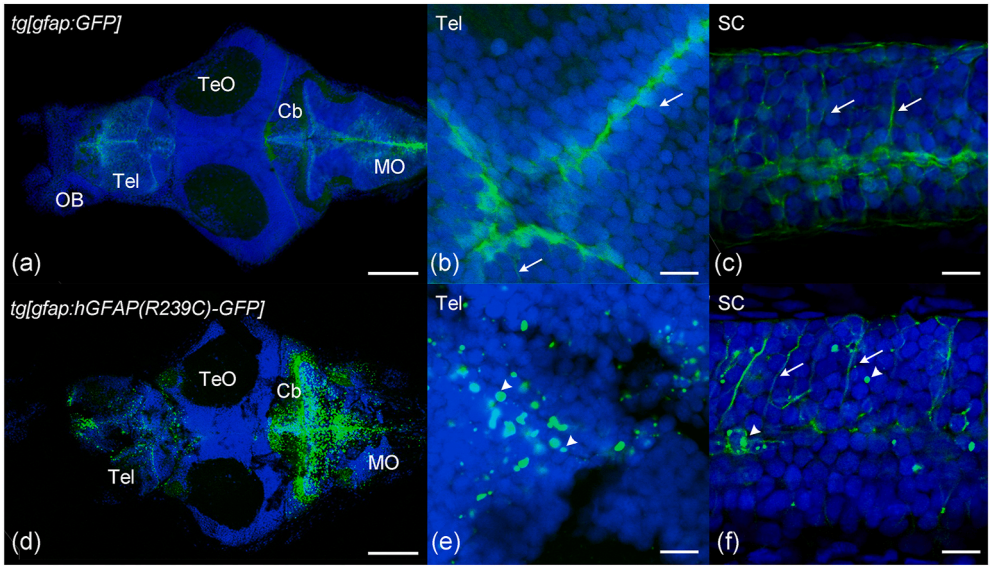

Name of the plasmid	Plasmid structure	Transgenic line
pTol2-gfap promoter:GFP	Tol2 — *gfap* promoter (zebrafish) — Flag Flag Flag — GFP — Tol2	Tg[gfap:GFP]mi2001 abbreviated as **gfap:GFP**
pTol2-GFAP(p.R239C)-GFP	Tol2 — *gfap* promoter (zebrafish) — p.R239C GFAP — Flag Flag Flag — GFP — Tol2	Tg[gfap:hGFAP(R239C)-GFP] abbreviated as **Tg(R239C-GFP)**

(g)

Fig. 1. Confocal images of Tg(gfap:GFP)mi2001 and the Tg(gfap:hGFAP(R239C)-GFP) transgenic zebrafish lines at 10 dpf. (**a**) Whole brain of a control Tg(gfap:GFP)mi2001 zebrafish larva at low magnification in dorsal view. (**b**,**c**) Enlargement of the telencephalic (**b**) and spinal cord (**c**) regions of the same larva showing the elongated pattern of GFP-positive cells (arrows). (**d**) Whole brain of a Tg(gfap:hGFAP(R239C)-GFP) zebrafish larva at low magnification in dorsal view. (**e**,**f**) Enlargement of the telencephalic (**e**) and spinal cord (**f**) regions of the same larva showing the presence of both GFP-positive aggregates (arrowheads) and the elongated pattern. In all panels, nuclei are shown in blue. The scale bar is 100 μm in panels **a** and **d**, and 10 μm in all other panels. Abbreviations: Cb, cerebellum; MO, medulla oblongata; OB, olfactory bulb; SC, spinal cord; Tel, telencephalon; TeO, tectum opticum. Plasmids used to generate transgenic lines are shown in (**g**).

In line with the findings of Bernandos and colleagues regarding the transgenic line Tg(gfap:GFP)mi2001 [28], our mutant transgenic line Tg (gfap:hGFAP(R239C)-GFP) exhibited a similar temporal and spatial distribution pattern in the nervous system, as illustrated in Fig. 2. Specifically, GFP expression became prominently evident in the developing brain and spinal cord by the 24 hpf stage, as depicted in Fig. 2a. Concurrently, GFP-expressing cells were discernible in the retina and lens at this stage. This expression pattern persisted through subsequent developmental stages, however, as mentioned before, the mutant line Tg (gfap:hGFAP(R239C)-GFP), exhibited a heightened presence of p. R239C-GFP aggregates at later stages, particularly notable at 10 dpf (Fig. 2b and c) and 20 dpf. These aggregates, previously characterized by TEM in our work [14], resemble the Rosenthal fibers found within astrocytes. The presence of GFAP aggregates in brain homogenates was investigated by western blot analysis which showed signals with higher molecular mass then expected, thus suggesting the formation of mutant GFAP oligomers in Tg(gfap:hGFAP(R239C)-GFP) (Supplementary Fig. 1). TUNEL assays confirmed that the GFAP aggregates in our AxD model are unrelated to neuronal degradation and originate from the speckled pattern of the mutant protein aggregates (Supplemental Fig. 2).

Furthermore, our immunohistochemical analysis revealed that p. R239C-GFP expression in larvae of 10 dpf and 20 dpf is specific to glial cells, as it displayed co-localization with anti-GFAP antibodies (Fig. 2h–k), while showing no co-localization with neuronal-specific antibodies such as HuC/D (Fig. 2d–g). To confirm the specificity of endogenous GFAP expression in zebrafish we used the same antibodies against HuC/D (Fig. 2l-o) and GFAP (Fig. 2p–s) on the Tg(gfap:GFP) mi2001 control line. In conclusion, our data unequivocally demonstrate the central nervous system-specific expression of pR239C-GFP, notably characterized by glial-specific expression.

Physiological conditions of our AxD model have been assessed performing electrophysiological recordings by high density micro electrode array (HD-MEA). Our preliminary data showed that the spontaneous activity recorded from Tg(gfap:GFP) control embryos displayed organized functional behaviors, with synchronized activity across different body regions. In contrast, in the case of Tg(hR239C-GFAP:GFP) embryos, a considerable increase in spiking activity was observed, resulting in a higher firing frequency. The mutated embryos also exhibited an increase in bursting activity at single channel land network level, with a significant extension in burst duration for Tg(hR239C-GFAP:GFP) compared to the controls, altering the normal physiological behavior (see Supplemental Fig. 3).

3.2. *RNA-seq analysis highlights the involvement of lipid-related processes and immune response in zAxD*

RNA-seq highlighted 503 differentially expressed genes (DEGs) among which 294 were down-regulated and 209 were up-regulated in zAxD larvae compared to controls (see Supplemental Table 1 for the complete list of DEGs). To confirm the validity of the RNA-seq data, we

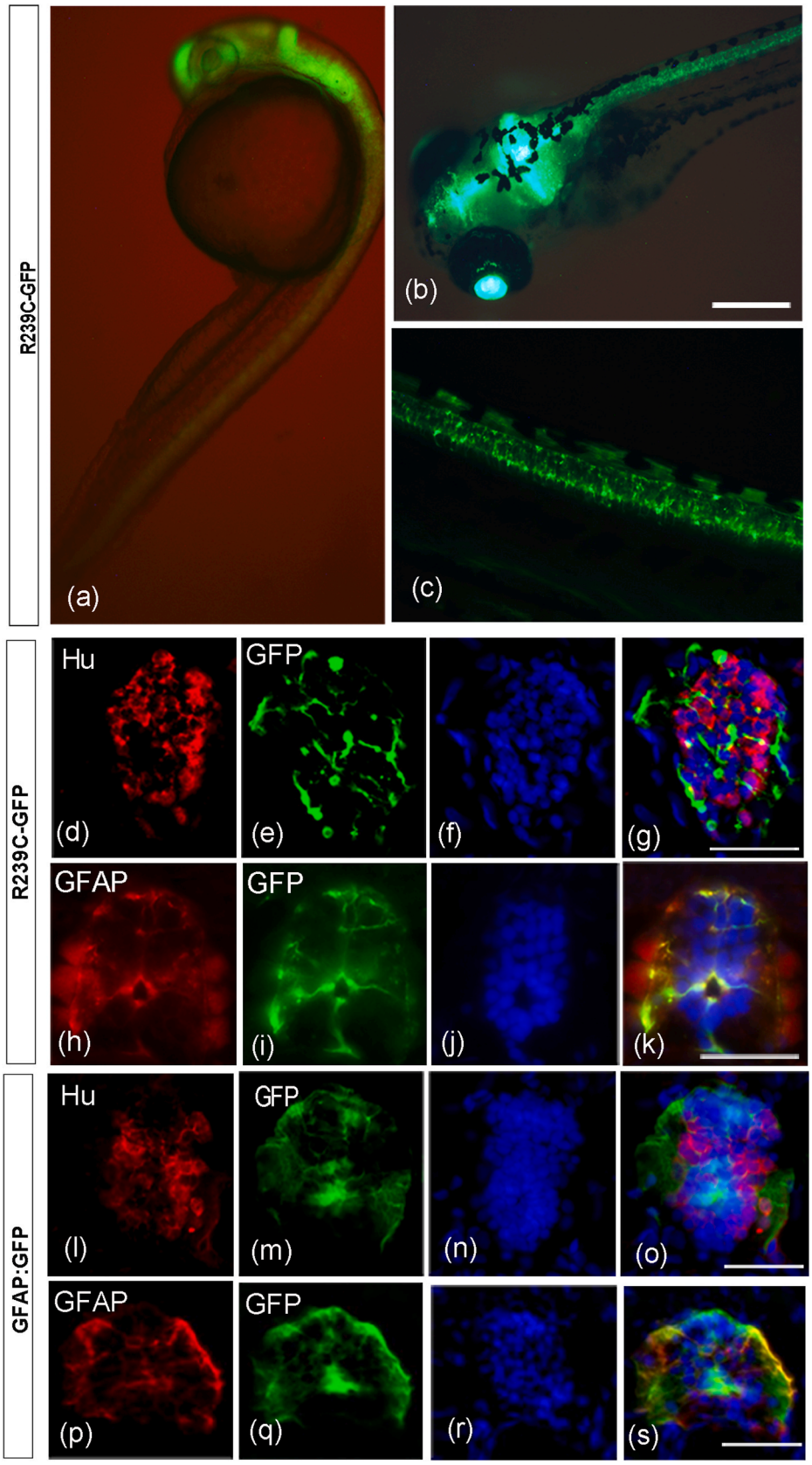

(caption on next page)

Fig. 2. Expression of GFP in the Tg(gfap:hGFAP(R239C)-GFP) transgenic zebrafish line at 24 hpf and 10 dpf. **(a)** Side view of a 24 hpf embryo. **(b)** anterior dorsal view of a 10 dpf larva, while **(c)** is a lateral view of the posterior part of the same larva. **(d–s)** GFP expression in larvae of Tg(gfap:hGFAP(R239C)-GFP) (indicated as R239C-GFP) and Tg(gfap:GFP)mi2001 (indicated as gfap:GFP) at 10 days post-fertilization (dpf) was analyzed alongside comparisons to glial and neuronal markers in cryosections of the brain. **(d)** Immunostaining with anti-HuC/D (red) revealed labeling of ventrolateral neurons in the brain, distinct from GFP-positive cells **(e)**. Merged imaging in **(g)** confirmed the absence of colocalization between anti-HuC/D and GFP signals. **(h)** Anti-GFAP staining (red) highlights intermediate filaments in the brain. **(t)** Cells labeled with anti-GFAP also exhibited GFP expression (green), as depicted in the overlay image **(k)**, indicating co-localization of anti-GFAP and GFP signals. **(l–o)** Immunostaining with anti-HuC/D (**l**, red) revealed labeling of ventrolateral neurons in the brain of gfap:GFP control line, distinct from GFP-positive cells lining the ventricle and extending processes towards the pial surface (**m**, green). Neither colocalization was visible in merged images (**o**). (**p-s**) Cells in the brain stained with the GFAP antibody (**p**) colocalized with GFP expressing cells (**q,s**). Labeled nuclei by Hoechst are shown in panels **f**, **j**, **n**, r. The scale bar is 50 μm in panels **a**, **d-s** and 100 μm in panels **c**, **b**.

validated two of the most differentially expressed genes by qRT-PCR, Ifit8 and Ifi27.1 (Supplemental Fig. 4).

Our pathway enrichment analyses revealed that among the statistically significant biological processes are mostly related to immune system activation (cytokine and interleukin production, T cell activation and proliferation), but also to lipid catabolic processes. Interestingly, pathways related to regulation of neurogenesis and glial cells proliferation, as well as reactive oxygen species (ROS) response emerged (Fig. 3a). Moreover, these results were further confirmed performing an analogue analysis using PANGEA (Supplemental Figs. 5A–C). The analysis of the molecular function (MF) highlighted the involvement of guanylate cyclase activator activity, GTP binding, transition metal ion binding, and NAD + ADP-ribosyltransferase activity, dopamine receptor activity and binding (Supplemental Fig. 5B). Furthermore, KEGG and Reactome analysis of DEGS at 10 dpf using PANGEA revealed the involvement of extracellular matrix organization and PPAR signaling pathway (Supplemental Fig. 5C).

3.3. The p.R239C GFAP mutant zebrafish shows susceptibility to time-dependent lipid peroxidation

Given the increased susceptibility to lipoperoxidation reported in model organisms carrying the R239C mutation [51], we examined the malondialdehyde (MDA) concentration at various stages of animal development in our model to gain insights into the timing of the onset and progression of damage. Data reported in Fig. 3b show that MDA in the Tg(gfap:hGFAP(R239C)-GFP) line was significantly higher at 72 hpf compared to the wild-type and Tg(gfap:GFP)mi2001 samples, suggesting that this age could correspond to the onset of the disease, at least from the point of view of oxidative stress. MDA accumulation continued to increase progressively with age until reaching a peak at 10 dpf and remained constant through 20 dpf. It is important to note that the gfap-GFP insertion alone did not result in MDA accumulation, as the observed values were identical to those of the wild-type.

3.4. RNA-seq analysis highlights the involvement of nervous system specific genes

We found that several DEGs are expressed in the nervous system of zebrafish, as documented in the ZFIN database (https://zfin.org/) and reported in Supplemental Table 1. Among the 504 DEGs identified, 120 are expressed in the zebrafish nervous system (indicated in pale orange and in yellow in the Supplemental Table 1), with 56 being upregulated and 64 downregulated in the mutant compared to the control line.

By examining zebrafish DEGs specific to the nervous system, we also identified homologous genes in humans that are involved in brain diseases (https://www.genecards.org/). In particular, 40 DEG (13 upregulated, 27 downregulated) are genes associated with several types of nervous system diseases.

Within DEGs, we identified 17 miRNAs with altered expression. Of these, 10 are expressed in the nervous system, with 7 showing upregulation (miR-9, miR-196b, miR-30d, miR-457b, miR-133c, miR-10d, miR-194b) and 3 displaying downregulation (miR-182, miR-150, miR-124).

In particular, by using WM-ISH we evaluated the expression of miR-124 since it is a pan-neural miRNA and its downregulation in zebrafish causes a reduction in the number of oligodendrocytes [52]. The WM-ISH confirmed reduced level of miR-124 expression in the mutant compared to the control at all stages analyzed (Fig. 4). Specifically, at the 24 and 72-h stages, there was a noticeable lack of expression in the spinal cord (Fig. 4 a,b,d,e), and at 10 dpf, the expression was shifted more anteriorly in the mutant compared to the control line (Fig. 4c–f).

3.5. Proteomics analysis confirms the dysregulation of lipid-related processes in our zAxD model and the emergence of other pathways

Mass spectrometry (MS) analyses revealed 270 differentially expressed proteins (DEPs) between the Tg(gfap:hGFAP(R239C)-GFP) and control lines at 10 dpf. Among these, 128 proteins were up-regulated and 142 down-regulated in the Tg(gfap:hGFAP(R239C)-GFP) mutant line. The same comparison made at 20 dpf highlighted 154 up-regulated proteins and 267 down-regulated proteins (see Supplemental Table 2 for the complete list of DEPs). To identify the dysregulated pathways in the mutant line compared to the reporter line, gene ontology (GO) enrichment analysis was performed using ShyniGO, Enrichr, REVIGO and PANGEA.

The analysis of GO terms at 10 dpf pointed out that the most deregulated biological processes are oxygen binding and transport, tyrosine metabolic processes and iron ion homeostasis (Supplemental Fig. 5D). Other pathways involved are: oxidoreductase activity, acyl-CoA oxidase activity and cargo receptor activity, autophagy and protein ubiquitination (Supplemental Fig. 5E and F). Moreover, REVIGO analysis of DEPs at 10 dpf highlighted the involvement of several pathways related to lipid metabolism, neuron migration and synaptic compartment (Fig. 5). These results were further confirmed by ShyniGO and Enrichr analysis (Supplemental Figs. 6A and C).

Interestingly, the GO terms related to lipid metabolic processes and lipid homeostasis were present in both RNA-seq and MS datasets at 10 dpf and persisted at the 20 dpf stage (Figs. 3a and 5). At 20 dpf, among the pathways emerging from REVIGO analysis there are regulation of neuron projection development, extracellular matrix organization, fatty acid beta oxidation and biosynthetic processes, regulation of cellular response to stress and regulation of macroautophagy (Fig. 5b).

These results were further confirmed by PANGEA Biological Process (BP), MF and KEGG/Reactome analysis. Moreover, both PANGEA BP and ShyniGO analyses highlighted the involvement of biological processes related to eye lens (Supplemental Figs. 5G and 6B), consistently with our finding of mutant GFAP aggregation also in the zAxD lens. Moreover, ShyniGO and Enrichr analyses pointed out the involvement of focal adhesion and butanoate metabolism pathways (Supplemental Figs. 6B and D).

While the enrichment of the pathways linked to lipid metabolism at 10 dpf persisted at 20 dpf (Fig. 6), the response to stress and immune response were found in the RNA-seq analysis at 10 dpf and in proteomics analysis only at 20 dpf (Supplemental Fig. 5).

3.6. Comparison with the in-silico zebrafish matrisome

To better investigate the role of extracellular matrix organization, which was identified as a new pathway by both transcriptomics and proteomics (Supplemental Fig. 5C and 5b), we compared our DEPs with

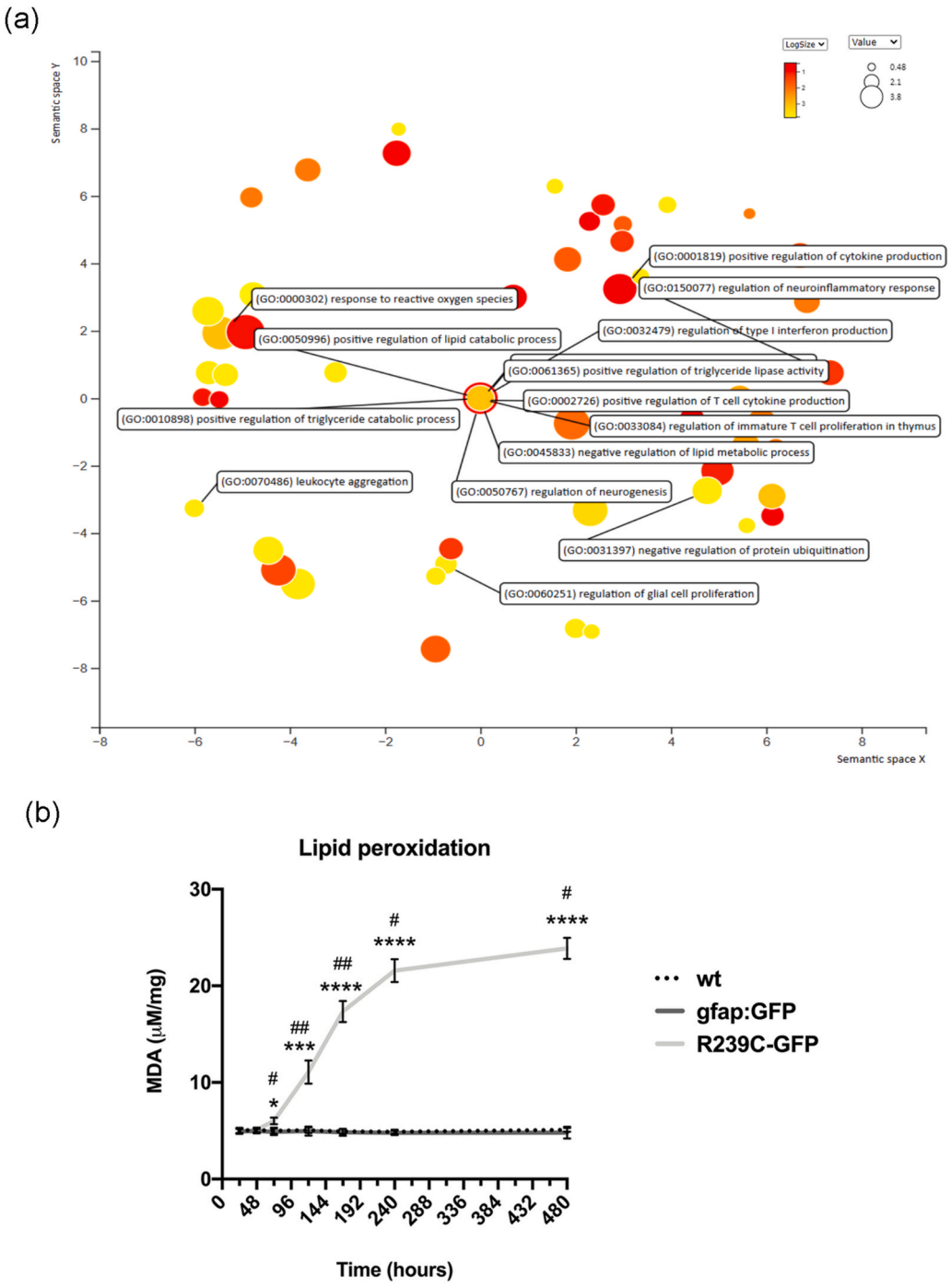

Fig. 3. **(a)** Scatterplot showing the most significant GO terms emerging from the RNA-seq in the zebrafish Tg(gfap:hGFAP(R239C)-GFP) larvae compared to Tg(gfap:GFP)mi2001 controls. Analysis was performed with Revigo, which uses multidimensional scaling (MDS) to reduce the dimensionality of a matrix of the GO terms pairwise semantic similarities. The resulting projection may be highly nonlinear. Connected similar GO terms remain close together in the plot; the semantic space units have no intrinsic meaning. Bubble color indicates the p-value for the false discovery rates; circle size indicates the frequency of the GO term in the underlying GO database, where bubbles of more general terms are larger. **(b)** Lipid peroxidation accumulation during animal development. The graph shows the intracellular MDA level in wild-type (wt), Tg(gfap:GFP)mi2001 (indicated as gfap:GFP), and Tg(gfap:hGFAP(R239C)-GFP) (indicated as R239C-GFP) larvae from 24 hpf to 20 dpf. Data represent 3 independent experiments (n = 3), and, for each experiment, n = 25 larvae were employed for each sample group). Statistical analysis between the three sample groups was performed with one-way ANOVA followed by Tukey's multiple comparisons test, for each time point analyzed. The difference between a time points and the previous one in the R239C-GFP sample was assessed with the *t*-test. Statistical significance between groups is reported as follows: ****/#### < 0.0001; * indicates comparisons between R239C-GFP and wt; # indicates comparisons between the animal's age and previous age in the same condition.

the in-silico zebrafish matrisome [53] (http://igfl.ens-lyon.fr/equipes/f.-ruggiero-matrix-biology-and-pathology/ZF-m@trix). In this work, Nauroy and collaborators used an in-silico gene-orthology-based approach to identify the zebrafish extracellular matrix (ECM) proteins and, with this approach, they were able to identify 1002 genes encoding the matrisome component. Moreover, they divide the entire matrisome into two main categories (core matrisome and matrisome-associated), each one composed of three subcategories (ECM glycoproteins, collagens, and proteoglycans for the core matrisome and ECM-affiliated proteins, ECM regulators and secreted factors for the

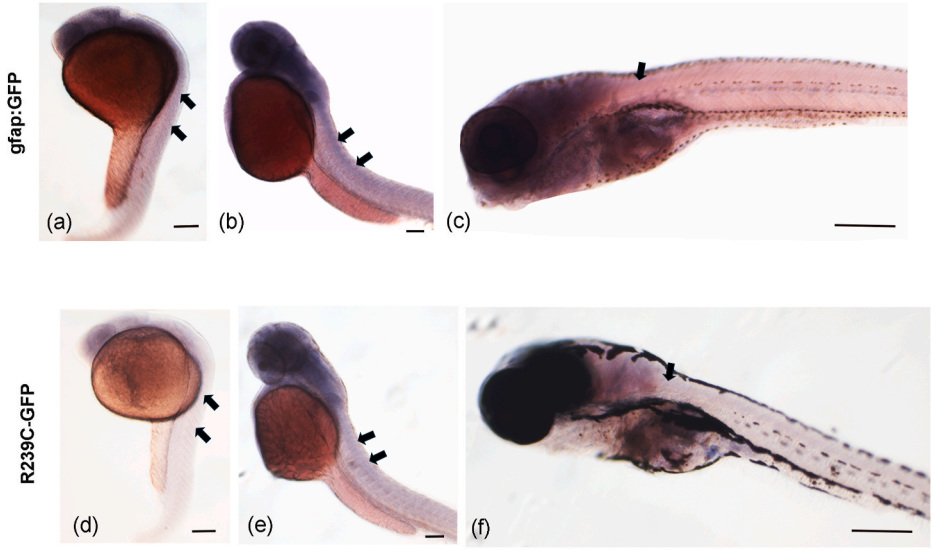

Fig. 4. Whole-mount in situ hybridization (ISH) with miR-124 LNA (Locked Nucleic Acid) probe on 24-hpf, 72-hpf and 10 dpf. Black arrows show presence (a, b, c) or absence (d, e, f) of miR-124 expression. Scale bar is 50 μm.

matrisome-associated). From this comparison, 42 of our DEPs (at 10 and 20 dpf) are present in the matrisome, representing 3,25 % of the matrisome's proteins. Among them, the majority (~24 %) belongs to collagens and ECM glycoproteins, followed by ECM regulators (~22 %) and, lastly, proteoglycans and ECM-affiliated proteins (~15 %).

3.7. Tg(gfap:hGFAP(R239C)-GFP) mutant zebrafish display altered aerobic metabolism and an unbalanced lipid metabolism towards fatty acids synthesis

To validate some of the data obtained by the omics approach, we investigated the impact of GFAP aggregation on OCR, ATP synthesis, and their ratio (P/O) in wild-type zebrafish, Tg(gfap:GFP)mi2001 reporter line and in the Tg(gfap:hGFAP(R239C)-GFP) line. Both the reporter line and wild-type zebrafish larvae produced energy and consumed oxygen (Fig. 7a) through oxidative phosphorylation at both 10 and 20 dpf. In contrast, Tg(gfap:hGFAP(R239C)-GFP) zebrafish larvae showed a decrement of about the 63 % of ATP synthesis and OCR in the presence of both pyruvate/malate (P/M) and succinate (Succ), suggesting an alteration in the mitochondrial metabolic functions. The ATP synthesis and OCR were further decreased by about 35 % in the mutant line at 20 dpf compared to 10 dpf. In addition, the efficiency of mitochondrial metabolism, calculated as the ratio of produced ATP to consumed oxygen (P/O ratio), showed lower values in Tg(gfap:hGFAP (R239C)-GFP) mutant zebrafish than in the reporter line and wild-type zebrafish (Fig. 7a), suggesting an uncoupling between energy production and cellular respiration, a condition that could explain the oxidative stress and damage increment associated with GFAP mutation. In addition, the reduction of the OxPhos efficiency appeared more severe at 20 dpf than at 10 dpf, although only for the P/M-induced pathway. Since the proteomics data indicated alterations in the lipid metabolism, the activity of 3-hydroxyacyl-CoA dehydrogenase and β-ketoacyl-ACP reductase were assayed as markers of fatty acids beta-oxidation and synthesis, respectively. While the activity of these two enzymes remained similar in wild-type and Tg(gfap:GFP)mi2001 larvae, Tg(gfap: hGFAP(R239C)-GFP) larvae showed a decrease of about two-fold in 3-hydroxy acyl-CoA dehydrogenase activity and an increase of about 50 % in β-ketoacyl-ACP reductase activity (Fig. 7b), both more marked at 20 dpf than 10 dpf. These data are indicative of a metabolic switch from fatty acid catabolism to synthesis.

3.8. Tg(gfap:hGFAP(R239C)-GFP) mutant zebrafish is characterized by oxidative damage not counteracted by enzymatic antioxidant defenses

Altered OxPhos function and partial uncoupling between respiration and ATP synthesis, are usually associated with an increment in reactive oxygen species (ROS) production, as altered monoelectronic transfers occurring in the electron transport chain are more likely to give rise to reactive oxygen species [45,54]. Therefore, we investigated oxidative stress levels in our zAxD.

In addition to the lipid peroxidation accumulation reported in Fig. 3c, Tg(gfap:hGFAP(R239C)-GFP) larvae showed elevated levels of superoxide anion compared to wild-types and the Tg(gfap:GFP)mi2001 line (Fig. 7c). Moreover, Tg(gfap:hGFAP(R239C)-GFP) mutant zebrafish displayed an increment of about 57 % of NADPH oxidase activity (Fig. 7c), which represents another source of oxidative stress. As with the alteration of aerobic and lipid metabolism, superoxide levels and NADPH oxidase activity also appeared to be higher in animals at 20 dpf than in those at 10 dpf. Interestingly, Tg(gfap:hGFAP(R239C)-GFP) mutant zebrafish were able to activate an adaptive response to increased oxidative stress by enhancing approximately twice the activity of catalase, glutathione reductase, and glutathione peroxidase, three enzymes involved in ROS detoxification (Fig. 7d). Again, the differences are more pronounced in the 20 dpf larvae than in the 10 dpf ones. However, the activation of these antioxidant defenses appeared insufficient to counterbalance oxidative stress as Tg(gfap:hGFAP(R239C)-GFP) mutant zebrafish showed a lipid peroxidation accumulation.

4. Discussion

In this work, we present the first multi-omics investigation performed in a zebrafish model of Alexander disease (AxD). The generation of a stable zebrafish transgenic line expressing the human *GFAP* gene carrying the p.R239C mutation in GFAP-positive glial cells allowed us to investigate the molecular mechanisms underlying AxD at later stages and with more detail compared to the mosaic model previously described [14]. The transgenic Tg(gfap:hGFAP(R239C)-GFP) larvae present aggregates throughout the central nervous system which are more abundant in the telencephalon and hindbrain. These brain regions are characterized by the highest activity of the *gfap* promoter, as demonstrated by the control Tg(gfap:GFP)mi2001 line in which, however, the aggregates are absent. Importantly, AxD mainly involves hindbrain structures and, to a lesser extent, the forebrain [5]. Therefore,

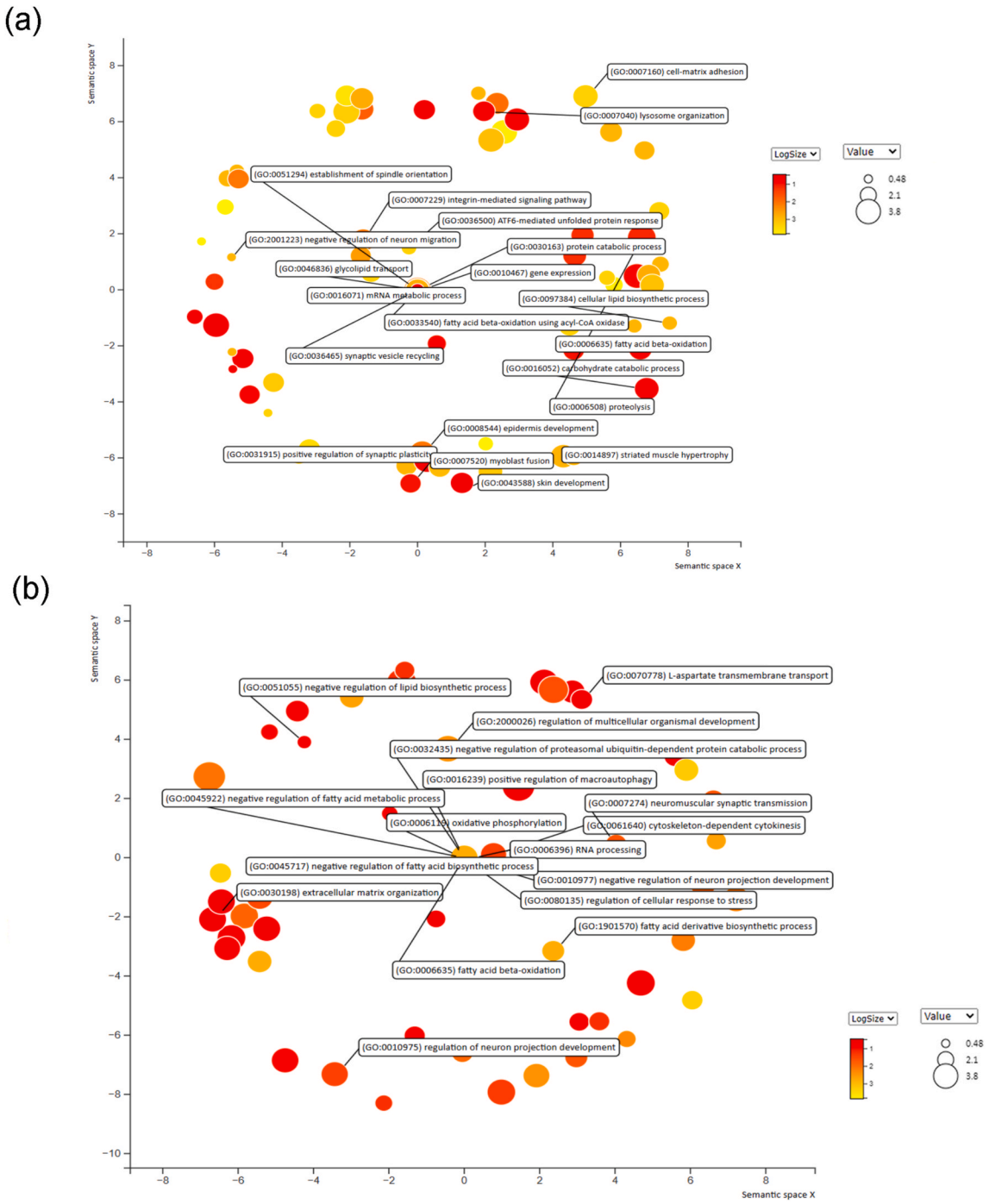

Fig. 5. **(a)** Scatterplot showing the most significant GO terms emerging from proteomic analysis at 10 dpf in the zebrafish Tg(gfap:hGFAP(R239C)-GFP) larvae compared to Tg(gfap:GFP)mi2001 controls. **(b)** Scatterplot showing the most significant GO terms emerging from proteomic analysis of 20-dpf Tg(gfap:hGFAP (R239C)-GFP) and Tg(gfap:GFP)mi2001 larvae. Analysis was performed with Revigo, which uses Multidimensional Scaling (MDS) to reduce the dimensionality of a matrix of the GO terms pairwise semantic similarities. The resulting projection may be highly nonlinear. Connected similar GO terms remain close together in the plot; the semantic space units have no intrinsic meaning. Bubble color indicates the p-value for the false discovery rates; circle size indicates the frequency of the GO term in the underlying GO database, where bubbles of more general terms are larger.

the localization of the aggregates in our zAxD model well recapitulates the areas of the human brain that are more strongly affected in AxD patients.

The use of the entire zebrafish organism, not feasible with other animal models because of their size, allowed us to disclose not only region-specific alterations directly ascribed to the expression of mutated GFAP in astrocytes but also broader dysregulations across the whole organism. We decided to use the entire organisms in line with several other omics works aimed at investigating the molecular pathogenesis of diseases related to the central nervous system, such as Amyotrophic Lateral Sclerosis and the leukodystrophy Vanishing white matter (VWM) disease. These studies have similarly employed whole zebrafish models to disclose altered pathways [55,56].

To better characterize AxD pathogenesis, we selected 10 dpf and 20 dpf time points of the development of our zAxD model. The rationale for this choice lies in both the early onset of p.R239C AxD and the timing of

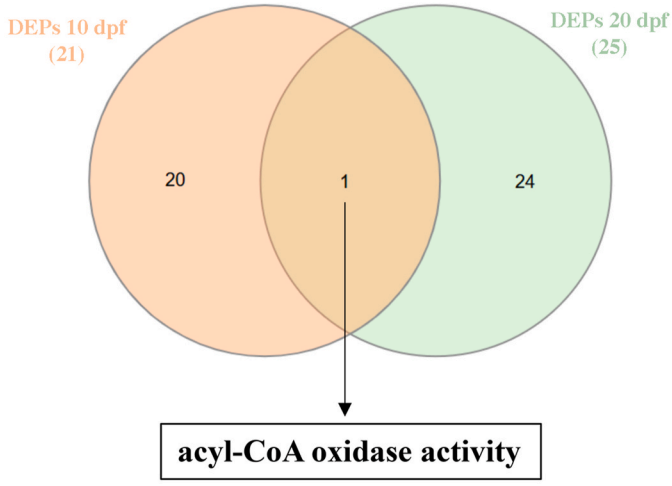

DEPs 10 dpf
oxygen binding
oxidoreductase activity, acting on single donors with incorporation of molecular oxygen
oxidoreductase activity, acting on single donors with incorporation of molecular oxygen, incorporation of two atoms of oxygen
dioxygenase activity
serine-type endopeptidase activity
serine-type peptidase activity
palmitoyl hydrolase activity
endopeptidase activity
peptide alpha-N-acetyltransferase activity
oxidoreductase activity, acting on other nitrogenous compounds as donors
transition metal ion binding
peptidase activity
oxidoreductase activity
iron ion binding
oxidoreductase activity
copper ion binding
thiolester hydrolase activity
oxidoreductase activity, acting on paired donors, with incorporation or reduction of molecular oxygen
endonuclease activity
cargo receptor activity

DEPs 20 dpf
transmembrane receptor protein tyrosine kinase activity
low-density lipoprotein particle receptor binding
lipoprotein particle receptor binding
glycosaminoglycan binding
collagen binding
tRNA binding
growth factor binding
proteoglycan binding
hydrolase activity
phosphatase activity
phosphoprotein phosphatase activity
hydrolase activity, acting on ester bonds
N-acyltransferase activity
phosphoric ester hydrolase activity
protein tyrosine kinase activity
histone acetyltransferase activity
insulin-like growth factor binding
hydrolase activity, acting on carbon-nitrogen (but not peptide) bonds, in linear amidines
peptide-lysine-N-acetyltransferase activity
endoribonuclease activity
protein disulfide oxidoreductase activity
RNA polymerase II proximal promoter sequence-specific DNA binding
proximal promoter sequence-specific DNA binding
nucleotidyltransferase activity

Fig. 6. Venn diagram, obtained with PANGEA, illustrating the biological processes emerging from proteomics analysis at 10 and 20 dpf in the mutant Tg(gfap:hGFAP (R239C)-GFP) compared to the control.

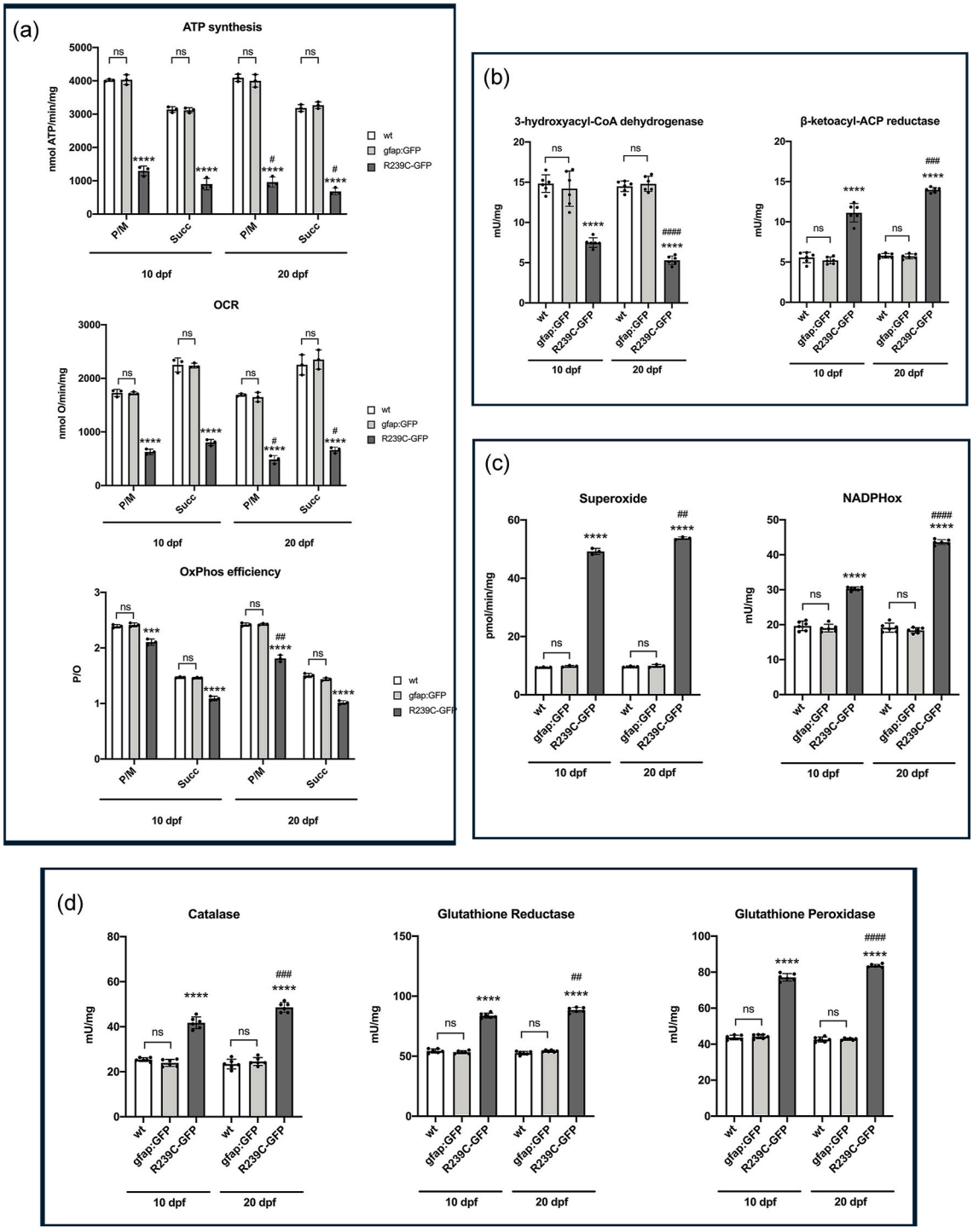

Fig. 7. **(a)** ATP synthesis, oxygen consumption rate (OCR), and the ratio between ATP synthesis and oxygen consumption (P/O) in wild-type (wt), Tg(gfap:GFP)mi2001 (indicated as gfap:GFP), and Tg(gfap:hGFAP(R239C)-GFP) (indicated as R239C-GFP) larvae at 10 and 20 dpf, induced by pyruvate plus malate (P/M) or succinate (Succ) as respiring substrates. Each panel is representative of n = 3 independent experiments and, for each experiment, n = 25 larvae were employed for each sample group. **(b)** 3-hydroxyacyl-CoA dehydrogenase and β-ketoacyl-ACP reductase activity in wild-type (wt), Tg(gfap:GFP)mi2001(indicated as gfap:GFP), and Tg(gfap:hGFAP(R239C)-GFP) (indicated as R239C-GFP) larvae at 10 and 20 dpf. Each panel is representative of n = 6 independent experiments and, for each experiment, n = 25 larvae were employed for each sample group. **(c)** Superoxide levels (n = 3 independent experiments), and NADPH oxidase activity (n = 6 independent experiments) in wild-type (wt), Tg(gfap:GFP)mi2001 (indicated as gfap:GFP), and Tg(gfap:hGFAP(R239C)-GFP) (indicated as R239C-GFP) larvae at 10 and 20 dpf. For each experiment, n = 25 larvae were employed for each sample group. **(d)** Catalase activity, glutathione reductase activity, and glutathione peroxidase activity in wild-type (wt), Tg(gfap:GFP)mi2001 (indicated as gfap:GFP), and Tg(gfap:hGFAP(R239C)-GFP) (indicated as R239C-GFP) larvae at 10 and 20 dpf. Panels are representative of n = 6 independent experiments, and, for each experiment, n = 25 larvae were employed for each sample group. Statistical analysis between the three sample groups was performed with one-way ANOVA followed by Tukey's multiple comparisons test, for each larvae stage. Statistical analysis on Tg(gfap:hGFAP(R239C)-GFP) between 10 or 20 dpf stages was performed by *t*-test. Statistical significance between groups is reported as follows: ns = not significant; */# = 0,01; **/## = 0,001; ***/### = 0,0001; ****/#### <0,0001. * = p value vs wt; # = p value R239C-GFP 10 dpf vs 20 dpf.

myelin formation in zebrafish. Since in the zebrafish brain myelination starts at around 4 dpf and the first heavily myelinated axons are found by 7 dpf [57], we were able to characterize the impact of the mutation both on early and late phases of the myelination process. Thus, the first time point of 10 dpf was chosen following the observation of metabolic alteration at this stage; the second one was used to monitor the trend of the disease.

To date, a few omics studies have been already performed focusing on cellular models of AxD or regions of the central nervous system. In particular, RNA-seq analysis was performed on hiPSC-derived astrocytes and brain tissue from AxD patients [16] as well as on the hippocampus and immunodepleted cerebrospinal fluid from transgenic mouse models of AxD [17,19]. On the other hand, proteomics analysis was performed on Rosenthal fibers from AxD patients and on the whole brain of a mouse model of the disease [8,18]. Several pathways emerged as dysregulated in these studies, such as immune system activation, cellular adhesion, ion transport, glial cell differentiation, synaptic transmission, and the PPAR pathway.

The transcriptomics analysis on our zAxD model highlighted a notable downregulation of several genes that are downstream of interferon signaling, suggesting the involvement of the immune response in this pathology, which is further corroborated by the analysis of the differentially expressed pathways. It has been recently reviewed the relevance of interferon α in several neurodegenerative diseases, exerting a neurotoxic effect and being involved in inflammatory processes [58]. Although the precise role of interferon in neurodegeneration is still under investigation, the involvement of the immune system and inflammatory response in AxD has already been reported in the hippocampus of a mouse model [19], and in both AxD iPSCs-induced astrocytes and brain tissue from AxD patients [16], thus confirming our findings and the validity of our model. Moreover, we observed that the immune system response biological processes were already modulated at 10 dpf and persisted to 20 dpf, suggesting a role in the progression of the disease.

Other interesting processes emerging at the 10 dpf stage are related to iron homeostasis, peroxidase activity, and tyrosine metabolic processes. Iron homeostasis is particularly relevant in the brain, likely due to the high iron levels in astrocytes, oligodendrocytes, and microglia [59]. Imbalances in iron levels can lead to neurobehavioral impairments, neuroinflammation, and neurodegeneration [60,61]. Furthermore, iron deficiency in OPC and mature oligodendrocytes appears to be related to myelination impairment [62]. Our zAxD model shows dysregulation of the iron metabolism pathway, previously reported to be altered in the brain of a mouse model of AxD [63]. Therefore, we hypothesize that myelination defects, typical of this disease, may also depend on iron dysmetabolism in oligodendrocytes. Since iron is a key component of cytochromes belonging to the electron transport chain, the alteration of iron metabolism can also explain, at least in part, the reduced oxygen consumption rate and ATP synthesis observed in our zAxD model.

Our data coming from electrophysiological analysis pointed out that R239C-GFP embryos showed a statistically significant increase in burst duration, while the control networks maintained a consistent pattern without significant changes in all body regions. Bursting activity is essential for establishing functional neuronal connections and promoting coordinated activity. However, uncontrolled or excessive bursting is a hallmark of epileptic brain activity and is considered seizure-like behavior in MEA recordings [64–66].

These findings suggest that dysregulation of astrocyte function can lead to profound neuronal dysfunction, potentially contributing to the pathogenesis of AxD.

Our transcriptomic analysis also reveals that several genes expressed in the zebrafish nervous system are differentially expressed and that many of them are associated with neurodegenerative diseases in humans. An additional interesting finding from this study is that many DEGs are brain-specific miRNAs not only in zebrafish but also in humans. Notably, miR-9 and miR-124 are two brain-specific miRNAs that are abundantly expressed in both developing and adult vertebrate brain and are both differentially expressed in our AxD model. In human, these miRNAs play a role in various biological functions within the central nervous system such as neuronal differentiation and function, including neurodegeneration, neuroimmune disorders, and stroke [67–69]. Interestingly, loss of miR-124 by morpholino knockdown in zebrafish, resulted in a reduction in oligodendrocyte cell numbers and impaired myelination of axonal projections in the ventral hindbrain [52].

Moreover, abnormal miR-124 expression has been identified in neural diseases such as Alzheimer's disease (AD), Parkinson's disease (PD), Huntington's disease (HD), hypoxic-ischemic encephalopathy, and ischemic stroke [70]. Furthermore, miR-124 provides protection in traumatic spinal cord injury by inhibiting M1 microglia and A1 astrocytes [71].

Several of the upregulated DEGs are associated with AD, and some have been shown to improve this pathological condition when inhibited, such as *scd* and *mmp9* [72,73]. Others, like *fosl1*, have been reported to suppress inflammation in BV-2 microglial cells and prevent the onset of epilepsy [74]. Furthermore, *lepa* and *lepb* have proven to exert neuroprotective role in AD [75,76], while *hsp90aa1,1* is likely involved in Aβ degradation via chaperone-mediated autophagy [77]. Several of the downregulated DEGs are associated with retinopathy and cone and crystalline dystrophy, such as *kcnv2b*, *guca1e* and *cyp4v7* ([78]; Georgiou et al., 2021; Han et al., 2022). Moreover, *faslg* is involved in both neuronal and immune cell apoptosis in AD [79] and *il21* has been proved to exacerbate AD pathology by escalating peripheral and brain immune and inflammatory responses leading to an increased Aβ plaque deposition. *Septin8b, tap2* and *gdf3* are involved in AD as well [80–82]. Lastly, some of the downregulated DEGs are involved in PD, such as *drd4b* [83] and *ptgdsb,2* which has been correlated with the NK pathway of cell-mediated cytotoxicity [71].

Reactive oxygen species and oxidative stress are among the factors contributing to neurodegeneration [84]. Notably, the brain consumes large amounts of oxygen, and neurons have a high content of polyunsaturated lipids, making them more susceptible to oxidation. Our experiments evaluating oxidative phosphorylation efficiency revealed an uncoupling between oxygen consumption and ATP synthesis in our zAxD model, a condition that is known to further promote ROS production. On the other hand, cells can activate several antioxidant responses to try to counterbalance an increase in oxidative stress production. Consistently, we found a general increase in the activity of detoxification enzymes, namely glutathione peroxidase, glutathione reductase, and catalase, in our zAxD model. These results are in line with the increased expression of these genes reported in a transgenic mouse model of AxD [85]. However, in our zAxD model, the increase in antioxidant enzyme activities was not sufficient to prevent the accumulation of oxidative membrane damage, as shown by the high levels of malondialdehyde. Interestingly, our zAxD model is the first *in vivo* model of AxD showing an elevated lipoxidation, which is in line with the *in vitro* findings [51]. The lipoperoxidation accumulation may also depend on the altered lipid metabolism. Indeed, we observed a decrease in beta-oxidation and an increase in fatty acid synthesis in our zAxD model, suggesting an adaptive response to the accumulation of acetyl-CoA that is not metabolized in the Krebs cycle due to the altered oxidative phosphorylation. In other words, the accumulation of fatty acids due to increased fatty acid synthesis could provide an increased substrate to perpetuate lipoperoxidation due to oxidative stress, which is not balanced by the increased antioxidant defenses.

These biochemical data are consistent with our proteomics dataset, which revealed a differential expression of some components of lipid metabolism associated with the PPAR signaling, such as *Sorbs1*, *Acadl* (*acyl-CoA dehydrogenase long chain*), and *Acox3* (*acyl-CoA oxidase 3*). Specifically, *Acadl* and *Acox3*, both involved in fatty acid beta-oxidation, were downregulated in zAxD. On the other hand, PPAR signaling is

known to be involved in AxD [18]. Furthermore, it has been recently reviewed that the fatty acids' β-oxidation is fundamental in brain homeostasis and a decreased fatty acid degradation may lead to neurodegeneration and neuroinflammation [86,87]. In addition, fatty acid β-oxidation plays a crucial role in oligodendrocytes, where this metabolic process allows the synthesis of myelin lipids [88]. Moreover, these observations confirm the role of lipid metabolism in AxD and open to further characterization of the dysregulated lipids as hypothetical biomarkers of this disease. Lipid peroxidation is well known to be involved in several neurodegenerative disorders, by inducing phospholipase activation which, in turn, plays a role in cell signaling as well as in ferroptosis and neuroinflammation [89,90]. Moreover, it has been reported that α-synuclein-induced cell death in PD is linked to lipid peroxidation [91]. High lipid peroxidation levels are also associated with other neurodegenerative pathologies like HD, where the lipid peroxidation biomarker 4-HNE co-localizes with mutant huntingtin protein (J. [92]), Friedreich's ataxia [93] and amyotrophic lateral sclerosis [94]. For all these reasons, lipid peroxidation may be considered as a potential therapeutic target for several neurodegenerative diseases and its intermediates are currently being studied as disease markers in AD and PD [95,96].

The connection between lipid dysmetabolism and myelin defects is particularly intriguing in AxD since it is classified as a leukodystrophy. It has been largely reported that several leukodystrophies are characterized by mutations occurring in genes involved in lipid metabolism pathways [97]. Moreover, it has been reported a leukodystrophy case in which mutations affecting the fatty acid metabolic pathway are associated with iron accumulation and neurodegeneration [98]. Therefore, even if AxD is not caused by mutations directly affecting lipid metabolic mechanisms, the previously reported findings, together with the multi-omics results from our zAxD model, strongly support the validity of our model. These findings allow us to speculate that the myelination defects typical of AxD may be at least partially attributed to the reported alterations in lipid metabolism and iron homeostasis.

In addition, concerning the altered lipid management, our data also reveal a defect in butanoate metabolism, a finding not previously reported in AxD. Nevertheless, several studies reported the involvement of butyrate, a short-chain fatty acid from which butanoate is derived, in reducing pro-inflammatory cytokines and improving synaptic plasticity in animal models of AD and PD [99–101]. Additionally, both *in vitro* and *in vivo* studies have highlighted the beneficial effect of butyrate on mitochondrial energy metabolism and oxidative stress reduction [102,103]. Furthermore, it has been reported that butanoate metabolism is downregulated in human reactive astrocytes [104]. Together, these findings suggest that butanoate metabolism may play a role in AxD pathogenesis.

Another pathway not previously associated with AxD is related to tyrosine metabolism. Tyrosine metabolism, crucial for the biosynthesis of some neurotransmitters, is altered also in other neurodegenerative diseases including HD, AD, and PD [105,106], suggesting that tyrosine could be a metabolic biomarker of AxD, as well as for other neurodegenerative diseases.

The focal adhesion pathway, including the ECM-receptor interaction term, ranks among the most represented categories in our proteome. These findings are consistent with the previously reported involvement of mechanotransduction signaling activation in *Drosophila* and mouse models of AxD, and in brain tissue from AxD patients [107]. Specifically, Lamin-A, a crucial player in mechanotransduction, is significantly increased in astrocytes of 3-month-old AxD model mice compared to age-matched control mice. Of note, in our zAxD model Lamin-A is one of the upregulated molecules, suggesting a potential role in modifying tissue stiffness as previously reported in other models [107,108]. Moreover, both ECM-receptor interaction and focal adhesion pathways also emerge from transcriptome analysis of human reactive astrocytes [104] as well as in zAxD, reinforcing the notion that mechanotransduction and ECM components play a role in AxD pathogenesis which is shared between different *in vivo*, and ex vivo models of this disease.

Very recently, a bioinformatic study based on results from omics studies performed on AxD and AD models has reported common features between the two pathologies [109].

In particular, in our model, we showed that ECM and iron pathways—identified as crucial in a 7-day zebrafish model of AD [110]—also seem to play a role in AxD, although at later stages, which could depend on the extent of GFAP mutation expression.

5. Conclusions

In this study we presented the first whole-organism multi-omics characterization of a zebrafish model of AxD. This approach allowed us to reveal the global alterations related to this disease and overcome the shortcomings of previous omics studies conducted on *in vitro* models of AxD or on specific organs. Among the enriched pathways emerging from the multi-omics analysis on our zAxD model, there are immune response and inflammatory response, iron homeostasis and peroxidation, focal adhesion and ECM-receptor interaction, PPAR signaling, and lipid metabolism. Biochemical assays confirmed alterations in cell respiration and lipid metabolism, as well as elevated oxidative stress. Moreover, dysregulation of neuro-gliogenesis pathways further attests to the reliability of the zebrafish model of neurodegenerative leukodystrophy. Additionally, new pathways have emerged from our analysis, such as tyrosine metabolic processes and butanoate metabolism opening to new investigations into metabolic processes and the interaction between astrocytes and the blood brain barrier in AxD.

These results confirm that a whole-organism approach is essential for better understanding the consequences of a complex disease like AxD.

Funding information

This research was supported by the Italian Association of Alexander disease "Più Unici che Rari" OdV to T.B. and S.C. This work has been supported by the Italian Ministry of Health "Ricerca Corrente" N.U733A to T.B.; by the Italian Ministry of Health (Ricerca Corrente) (grant number RF-2021-12374376) and the Italian Ministry of Health 5 × 1000 funds 2021 (grant number 5M-2021-23683841) to N.B., by the EOSC Life (R236A) to C.R., by University of Genoa (FRA 2023) to M.B.

CRediT authorship contribution statement

Deianira Bellitto: Writing – review & editing, Writing – original draft, Methodology, Investigation. **Matteo Bozzo:** Writing – review & editing, Writing – original draft, Methodology, Investigation. **Silvia Ravera:** Writing – original draft, Methodology, Investigation. **Nadia Bertola:** Methodology, Investigation. **Francesca Rosamilia:** Methodology, Investigation. **Jessica Milia:** Methodology, Investigation. **Paola Barboro:** Methodology, Investigation. **Gabriela Coronel Vargas:** Methodology, Investigation. **Donatella Di Lisa:** Methodology, Investigation. **Laura Pastorino:** Methodology, Investigation. **Francesca Lantieri:** Methodology, Investigation. **Patrizio Castagnola:** Methodology, Investigation. **Erika Iervasi:** Methodology, Investigation. **Marco Ponassi:** Methodology, Investigation. **Aldo Profumo:** Methodology, Investigation. **Kateryna Tkachenko:** Methodology, Investigation. **Camillo Rosano:** Supervision. **Simona Candiani:** Writing – review & editing, Writing – original draft, Validation, Supervision, Project administration, Funding acquisition, Formal analysis, Conceptualization. **Tiziana Bachetti:** Writing – review & editing, Writing – original draft, Validation, Supervision, Project administration, Funding acquisition, Formal analysis, Conceptualization.

Declaration of competing interest

None.

Acknowledgements

We are grateful to Seok-Yong Choi of the Department of Biomedical Sciences, Chonnam National University Medical School (Republic of Korea) for providing the pCS-TP, pTol2-GFAP (p.R239C)-GFP, and pTol2-gfap promoter-GFP plasmids and to the CEBR of the University of Genoa (Italy) for granting access to the Nikon AX R confocal microscope.

Appendix A. Supplementary data

Supplementary data to this article can be found online at https://doi.org/10.1016/j.redox.2025.103544.

Data availability

The data that supports the findings of this study are available in the supplementary material of this article. Furthermore, the RNA data are available at Genbank (https://www.ncbi.nlm.nih.gov/genbank/) under accession number PRJNA1034091 (BioSample: SAMN38050941 and SAMN38050940).

Proteomic data are available at the PRIDE repository (https://www.ebi.ac.uk/pride/archive/) with the dataset identifier PXD040214 (DOI: 10.6019/PXD040214).

References

[1] W.S. Alexander, Progressive fibrinoid degeneration of fibrillary astrocytes associated with mental retardation in a hydrocephalic infant, Brain 72 (3) (1949) 373–381, https://doi.org/10.1093/brain/72.3.373.

[2] M. Prust, J. Wang, H. Morizono, A. Messing, M. Brenner, E. Gordon, T. Hartka, A. Sokohl, R. Schiffmann, H. Gordish-Dressman, R. Albin, H. Amartino, K. Brockman, A. Dinopoulos, M.T. Dotti, D. Fain, R. Fernandez, J. Ferreira, J. Fleming, A. Vanderver, GFAP mutations, age at onset, and clinical subtypes in Alexander disease, Neurology 77 (13) (2011) 1287–1294, https://doi.org/10.1212/WNL.0b013e3182309f72.

[3] L.S. Russo, A. Aron, P.J. Anderson, Alexander's disease: a report and reappraisal, Neurology 26 (7) (1976) 607, https://doi.org/10.1212/WNL.26.7.607, 607.

[4] M. Brenner, A.B. Johnson, O. Boespflug-Tanguy, D. Rodriguez, J.E. Goldman, A. Messing, Mutations in GFAP, encoding glial fibrillary acidic protein, are associated with Alexander disease, Nat. Genet. 27 (1) (2001) 117–120, https://doi.org/10.1038/83679.

[5] A. Messing, Alexander disease, in: Handbook of Clinical Neurology, first ed., Elsevier B.V, 2018 https://doi.org/10.1016/B978-0-444-64076-5.00044-2, 148.

[6] A. Messing, C.M.L. Daniels, T.L. Hagemann, Strategies for treatment in alexander disease, Neurotherapeutics 7 (4) (2010) 507–515.

[7] R.A. Quinlan, M. Brenner, J.E. Goldman, A. Messing, MCF7 GFAP and its role in AxD, Cell 313 (10) (2009) 2077–2087, https://doi.org/10.1016/j.yexcr.2007.04.004.GFAP.

[8] M.R. Heaven, D. Flint, S.M. Randall, A.A. Sosunov, L. Wilson, S. Barnes, J. E. Goldman, D.C. Muddiman, M. Brenner, Composition of rosenthal fibers, the protein aggregate hallmark of alexander disease, J. Proteome Res. 15 (7) (2016) 2265–2282, https://doi.org/10.1021/acs.jproteome.6b00316.

[9] T. Iwaki, A. Iwaki, J. Tateishi, Y. Sakaki, J.E. Goldman, Alpha B-crystallin and 27-kd heat shock protein are regulated by stress conditions in the central nervous system and accumulate in Rosenthal fibers, Am. J. Pathol. 143 (2) (1993) 487–495.

[10] R. Li, A. Messing, J.E. Goldman, M. Brenner, GFAP mutations in Alexander disease, Int. J. Dev. Neurosci. 20 (3–5) (2002) 259–268, https://doi.org/10.1016/S0736-5748(02)00019-9.

[11] G. Tang, M.D. Perng, S. Wilk, R. Quinlan, J.E. Goldman, Oligomers of mutant glial fibrillary acidic protein (GFAP) inhibit the proteasome system in alexander disease astrocytes, and the small heat shock protein αB-crystallin reverses the inhibition, J. Biol. Chem. 285 (14) (2010) 10527–10537, https://doi.org/10.1074/jbc.M109.067975.

[12] A. Messing, M. Brenner, GFAP: functional implications gleaned from studies of genetically engineered mice, Glia 43 (1) (2003) 87–90, https://doi.org/10.1002/glia.10219.

[13] T. Bachetti, E. Di Zanni, P. Balbi, P. Bocca, I. Prigione, G.A. Deiana, A. Rezzani, I. Ceccherini, G. Sechi, In vitro treatments with ceftriaxone promote elimination of mutant glial fibrillary acidic protein and transcription down-regulation, Exp. Cell Res. 316 (13) (2010) 2152–2165, https://doi.org/10.1016/j.yexcr.2010.05.005.

[14] S. Candiani, S. Carestiato, A.F. Mack, D. Bani, M. Bozzo, V. Obino, M. Ori, F. Rosamilia, M. De Sarlo, M. Pestarino, I. Ceccherini, T. Bachetti, Alexander disease modeling in zebrafish: an in vivo system suitable to perform drug screening, Genes 11 (12) (2020) 1–19, https://doi.org/10.3390/genes11121490.

[15] W. Cho, M. Brenner, N. Peters, A. Messing, Drug screening to identify suppressors of GFAP expression, Hum. Mol. Genet. 19 (16) (2010) 3169–3178, https://doi.org/10.1093/hmg/ddq227.

[16] L. Li, E. Tian, X. Chen, J. Chao, J. Klein, Q. Qu, G. Sun, G. Sun, Y. Huang, C. D. Warden, P. Ye, L. Feng, X. Li, Q. Cui, A. Sultan, P. Douvaras, V. Fossati, N. E. Sanjana, A.D. Riggs, Y. Shi, GFAP mutations in astrocytes impair oligodendrocyte progenitor proliferation and myelination in an hiPSC model of alexander disease, Cell Stem Cell 23 (2) (2018) 239–251.e6, https://doi.org/10.1016/j.stem.2018.07.009.

[17] R. Cunningham, P. Jany, A. Messing, L. Li, Protein changes in immunodepleted cerebrospinal fluid from a transgenic mouse model of alexander disease detected using mass spectrometry, J. Proteome Res. 12 (2) (2013) 719–728, https://doi.org/10.1021/pr300785h.

[18] M.R. Heaven, A.W. Herren, D.L. Flint, N.L. Pacheco, J. Li, A. Tang, F. Khan, J. E. Goldman, B.S. Phinney, M.L. Olsen, Metabolic enzyme alterations and astrocyte dysfunction in a murine model of alexander disease with severe reactive gliosis, Mol. Cell. Proteomics 21 (1) (2022) 100180, https://doi.org/10.1016/j.mcpro.2021.100180.

[19] M. Olabarria, M. Putilina, E.C. Riemer, J.E. Goldman, Astrocyte pathology in Alexander disease causes a marked inflammatory environment, Acta Neuropathol. 130 (4) (2015) 469–486, https://doi.org/10.1007/s00401-015-1469-1.

[20] K. Chia, A. Klingseisen, D. Sieger, J. Priller, Zebrafish as a model organism for neurodegenerative disease, Front. Mol. Neurosci. 15 (2022) 1–27, https://doi.org/10.3389/fnmol.2022.940484.

[21] D. Corallo, M. Donadon, M. Pantile, V. Sidarovich, S. Cocchi, M. Ori, M. De Sarlo, S. Candiani, C. Frasson, M. Distel, A. Quattrone, C. Zanon, G. Basso, G.P. Tonini, S. Aveic, LIN28B increases neural crest cell migration and leads to transformation of trunk sympathoadrenal precursors, Cell Death Differ. 27 (4) (2020) 1225–1242.

[22] K. Dooley, L.I. Zon, Zebrafish: a model system for the study of human disease, Curr. Opin. Genet. Dev. 10 (3) (2000) 252–256, https://doi.org/10.1016/S0959-437X(00)00074-5.

[23] K. Howe, M.D. Clark, C.F. Torroja, J. Torrance, C. Berthelot, M. Muffato, J. E. Collins, S. Humphray, K. McLaren, L. Matthews, S. McLaren, I. Sealy, M. Caccamo, C. Churcher, C. Scott, J.C. Barrett, R. Koch, G.-J. Rauch, S. White, D. L. Stemple, The zebrafish reference genome sequence and its relationship to the human genome, Nature 496 (7446) (2013) 498–503, https://doi.org/10.1038/nature12111.

[24] A.L. Nielsen, A.L. Jørgensen, Structural and functional characterization of the zebrafish gene for glial fibrillary acidic protein, GFAP, Gene 310 (1–2) (2003) 123–132, https://doi.org/10.1016/S0378-1119(03)00526-2.

[25] R. Schmidt, U. Strähle, S. Scholpp, Neurogenesis in zebrafish – from embryo to adult, Neural Dev. 8 (1) (2013) 3, https://doi.org/10.1186/1749-8104-8-3.

[26] N. Jurisch-yaksi, Radial glia in the zebrafish brain: functional , structural , and physiological comparison with the mammalian glia, Glia 68 (12) (2020) 2451–2470, https://doi.org/10.1002/glia.23849.

[27] S.H. Lee, T.S. Nam, K.H. Kim, J.H. Kim, W. Yoon, S.H. Heo, M.J. Kim, B.A. Shin, M. Der Perng, H.E. Choy, J. Jo, M.K. Kim, S.Y. Choi, Aggregation-prone GFAP mutation in Alexander disease validated using a zebrafish model, BMC Neurol. 17 (1) (2017) 1–9, https://doi.org/10.1186/s12883-017-0938-7.

[28] R.L. Bernardos, P.A. Raymond, GFAP transgenic zebrafish, Gene Expr. Patterns 6 (8) (2006) 1007–1013, https://doi.org/10.1016/j.modgep.2006.04.006.

[29] K. Kawakami, Tol2: a versatile gene transfer vector in vertebrates, Genome Biol. 8 (S1) (2007) 1–10, https://doi.org/10.1186/gb-2007-8-s1-s7.

[30] C. Mosimann, L.I. Zon, Advanced zebrafish transgenesis with Tol2 and application for Cre/lox recombination experiments, Methods Cell Biol. 104 (2011) 173–194, https://doi.org/10.1016/B978-0-12-374814-0.00010-0.

[31] M. Bozzo, S. Candiani, M. Schubert, Whole mount in situ hybridization and immunohistochemistry for studying retinoic acid signaling in developing amphioxus, in: Methods in Enzymology, first ed., Elsevier Inc, 2020 https://doi.org/10.1016/bs.mie.2020.03.007, 637.

[32] J. Schindelin, I. Arganda-Carreras, E. Frise, V. Kaynig, M. Longair, T. Pietzsch, S. Preibisch, C. Rueden, S. Saalfeld, B. Schmid, J.-Y. Tinevez, D.J. White, V. Hartenstein, K. Eliceiri, P. Tomancak, A. Cardona, Fiji: an open-source platform for biological-image analysis, Nat. Methods 9 (7) (2012) 676–682, https://doi.org/10.1038/nmeth.2019.

[33] S.M. Peterson, J.L. Freeman, RNA isolation from embryonic zebrafish and cDNA synthesis for gene expression analysis, JoVE J. 30 (2009) 4–9, https://doi.org/10.3791/1470.

[34] B. Batut, M. van den Beek, M.A. Doyle, N. Soranzo, RNA-seq data analysis in Galaxy, Methods Mol. Biol. 2284 (2021) 367–392, https://doi.org/10.1007/978-1-0716-1307-8_20.

[35] M.I. Love, W. Huber, S. Anders, Moderated estimation of fold change and dispersion for RNA-seq data with DESeq2, Genome Biol. 15 (2014) 550, https://doi.org/10.1186/s13059-014-0550-8.

[36] M. Lawrence, W. Huber, H. Pagès, P. Aboyoun, M. Carlson, R. Gentleman, M. T. Morgan, V.J. Carey, Software for computing and annotating genomic ranges, PLoS Comput. Biol. 9 (8) (2013) e1003118, https://doi.org/10.1371/journal.pcbi.1003118.

[37] M. Morgan, J. Wang, V. Obenchain, M. Lang, R. Thompson, N. Turaga, BiocParallel: Bioconductor facilities for parallel evaluation, R package version 1.40.0 (2024). https://github.com/Bioconductor/BiocParallel.

[38] Y. Chen, L. Chen, A.T.L. Lun, P. Baldoni, G.K. Smyth, edgeR 4.0: powerful differential analysis of sequencing data with expanded functionality and

improved support for small counts and larger datasets, bioRxiv (2024), https://doi.org/10.1101/2024.01.21.576131.
[39] Y. Perez-Riverol, J. Bai, C. Bandla, D. García-Seisdedos, S. Hewapathirana, S. Kamatchinathan, D.J. Kundu, A. Prakash, A. Frericks-Zipper, M. Eisenacher, M. Walzer, S. Wang, A. Brazma, J.A. Vizcaíno, The PRIDE database resources in 2022: a hub for mass spectrometry-based proteomics evidences, Nucleic Acids Res. 50 (D1) (2022) D543–D552, https://doi.org/10.1093/nar/gkab1038.
[40] J. Doblmann, F. Dusberger, R. Imre, O. Hudecz, F. Stanek, K. Mechtler, G. Dürnberger, apQuant: accurate label-free quantification by quality filtering, J. Proteome Res., acs. jproteome.8b00113 (2018), https://doi.org/10.1021/acs.jproteome.8b00113.
[41] A.R.J. Alexa, topGO: enrichment analysis for gene ontology (2.54.0), R package (2023). https://bioconductor.org/packages/release/bioc/html/topGO.html.
[42] F. Supek, M. Bošnjak, N. Škunca, T. Šmuc, REVIGO summarizes and visualizes long lists of gene ontology terms, PLoS One 6 (7) (2011) e21800, https://doi.org/10.1371/journal.pone.0021800.
[43] M.M. Bradford, A rapid and sensitive method for the quantitation of microgram quantities of protein utilizing the principle of protein-dye binding, Anal. Biochem. 72 (1–2) (1976) 248–254, https://doi.org/10.1016/0003-2697(76)90527-3.
[44] P.C. Hinkle, P/O ratios of mitochondrial oxidative phosphorylation, Biochim. Biophys. Acta Bioenerg. 1706 (1–2) (2005) 1–11, https://doi.org/10.1016/j.bbabio.2004.09.004.
[45] S. Ravera, M. Podestà, F. Sabatini, M. Dagnino, D. Cilloni, S. Fiorini, A. Barla, F. Frassoni, Discrete changes in glucose metabolism define aging, Sci. Rep. 9 (1) (2019) 10347, https://doi.org/10.1038/s41598-019-46749-w.
[46] N. Bertola, P. Degan, E. Cappelli, S. Ravera, Mutated FANCA gene role in the modulation of energy metabolism and mitochondrial dynamics in head and neck squamous cell carcinoma, Cells 11 (15) (2022) 2353, https://doi.org/10.3390/cells11152353.
[47] H.U. Bergmeyer, in: H.U. Bergmeyer (Ed.), Methods of Enzymatic Analysis, vol. 2, 1974. Second.
[48] A.S. Veskoukis, N.V. Margaritelis, A. Kyparos, V. Paschalis, M.G. Nikolaidis, Spectrophotometric assays for measuring redox biomarkers in blood and tissues: the NADPH network, Redox Rep. 23 (1) (2018) 47–56, https://doi.org/10.1080/13510002.2017.1392695.
[49] M.G. Signorello, S. Ravera, G. Leoncini, Endocannabinoids effect on oxidative status of human platelets, J. Cell. Biochem. 124 (1) (2023) 46–58, https://doi.org/10.1002/jcb.30341.
[50] E. Cappelli, P. Degan, S. Bruno, F. Pierri, M. Miano, F. Raggi, P. Farruggia, C. Mecucci, B. Crescenzi, V. Naim, C. Dufour, S. Ravera, The passage from bone marrow niche to bloodstream triggers the metabolic impairment in Fanconi Anemia mononuclear cells, Redox Biol. 36 (2020) 101618, https://doi.org/10.1016/j.redox.2020.101618.
[51] Á. Viedma-Poyatos, P. González-Jiménez, M.A. Pajares, D. Pérez-Sala, Alexander disease GFAP R239C mutant shows increased susceptibility to lipoxidation and elicits mitochondrial dysfunction and oxidative stress, Redox Biol. 55 (2022) 102415, https://doi.org/10.1016/j.redox.2022.102415.
[52] J.K. Morris, A. Chomyk, P. Song, N. Parker, S. Deckard, B.D. Trapp, S. W. Pimplikar, R. Dutta, Decrease in levels of the evolutionarily conserved microRNA miR-124 affects oligodendrocyte numbers in Zebrafish, Danio rerio, Invertebr. Neurosci. 15 (3) (2015) 4, https://doi.org/10.1007/s10158-015-0180-1.
[53] P. Nauroy, S. Hughes, A. Naba, F. Ruggiero, The in-silico zebrafish matrisome: a new tool to study extracellular matrix gene and protein functions, Matrix Biol. 65 (2018) 5–13, https://doi.org/10.1016/j.matbio.2017.07.001.
[54] S. Ravera, M. Bartolucci, D. Calzia, A.M. Morelli, I. Panfoli, Efficient extra-mitochondrial aerobic ATP synthesis in neuronal membrane systems, J. Neurosci. Res. 99 (9) (2021) 2250–2260, https://doi.org/10.1002/jnr.24865.
[55] A.K. Frøyset, E.A. Khan, K.E. Fladmark, Quantitative proteomics analysis of zebrafish exposed to sub-lethal dosages of β-methyl-amino-L-alanine (BMAA), Sci. Rep. 6 (1) (2016) 29631, https://doi.org/10.1038/srep29631.
[56] D. Kim, Y.-R. Lee, T.-I. Choi, S.-H. Kim, H.-C. Kang, C.-H. Kim, S. Lee, Comparative proteome research in a zebrafish model for vanishing white matter disease, Int. J. Mol. Sci. 22 (5) (2021) 2707, https://doi.org/10.3390/ijms22052707.
[57] C. Brösamle, M.E. Halpern, Characterization of myelination in the developing zebrafish, Glia 39 (1) (2002) 47–57, https://doi.org/10.1002/glia.10088.
[58] B.S.M. Hui, L.R. Zhi, T. Retinasamy, A. Arulsamy, C.S.W. Law, Mohd F. Shaikh, K. Y. Yeong, The role of interferon-α in neurodegenerative diseases, Syst. Rev. J. Alzheimer's Dis. 94 (s1) (2023) S45–S66, https://doi.org/10.3233/JAD-221081.
[59] A. Reinert, M. Morawski, J. Seeger, T. Arendt, T. Reinert, Iron concentrations in neurons and glial cells with estimates on ferritin concentrations, BMC Neurosci. 20 (1) (2019) 25, https://doi.org/10.1186/s12868-019-0507-7.
[60] B. Lozoff, J. Beard, J. Connor, B. Felt, M. Georgieff, T. Schallert, Long-lasting neural and behavioral effects of iron deficiency in infancy, Nutr. Rev. 64 (5 SUPPL. 1) (2006), https://doi.org/10.1301/nr.2006.may.S34-S43.
[61] F. Molina-Holgado, R.C. Hider, A. Gaeta, R. Williams, P. Francis, Metals ions and neurodegeneration, Biometals 20 (3–4) (2007) 639–654, https://doi.org/10.1007/s10534-006-9033-z.
[62] E. Stephenson, N. Nathoo, Y. Mahjoub, J.F. Dunn, V.W. Yong, Iron in multiple sclerosis: roles in neurodegeneration and repair, Nat. Rev. Neurol. 10 (8) (2014) 459–468, https://doi.org/10.1038/nrneurol.2014.118.
[63] T.L. Hagemann, J.X. Connor, A. Messing, Alexander disease-associated glial fibrillary acidic protein mutations in mice induce Rosenthal fiber formation and a white matter stress response, J. Neurosci. 26 (43) (2006) 11162–11173, https://doi.org/10.1523/JNEUROSCI.3260-06.2006.
[64] A. Odawara, H. Katoh, N. Matsuda, I. Suzuki, Induction of long-term potentiation and depression phenomena in human induced pluripotent stem cell-derived cortical neurons, Biochem. Biophys. Res. Commun. 469 (4) (2016) 856–862, https://doi.org/10.1016/j.bbrc.2015.12.087.
[65] S.A. Chong, S. Balosso, C. Vandenplas, G. Szczesny, E. Hanon, K. Claes, X. Van Damme, B. Danis, J. Van Eyll, C. Wolff, A. Vezzani, R.M. Kaminski, I. Niespodziany, Intrinsic inflammation is a potential anti-epileptogenic target in the organotypic hippocampal slice model, Neurotherapeutics: J. Am. Soc. Experiment. NeuroTherapeut. 15 (2) (2018) 470–488, https://doi.org/10.1007/s13311-018-0607-6.
[66] Y. Liu, A.F. McGuire, H.Y. Lou, T.L. Li, J.B. Tok, B. Cui, Z. Bao, Soft conductive micropillar electrode arrays for biologically relevant electrophysiological recording, Proc. Natl. Acad. Sci. U. S. A 115 (46) (2018) 11718–11723, https://doi.org/10.1073/pnas.1810827115.
[67] H. Weng, C. Shen, G. Hirokawa, X. Ji, R. Takahashi, K. Shimada, C. Kishimoto, N. Iwai, Plasma miR-124 as a biomarker for cerebral infarction, Biomed. Res. 32 (2) (2011) 135–141.
[68] Q. Ji, Y. Ji, J. Peng, X. Zhou, X. Chen, H. Zhao, T. Xu, L. Chen, Y. Xu, Increased brain-specific MiR-9 and MiR-124 in the serum exosomes of acute ischemic stroke patients, PLoS One 11 (9) (2016) e0163645, https://doi.org/10.1371/journal.pone.0163645.
[69] C.A. Juźwik, S. Drake, Y. Zhang, N. Paradis-Isler, A. Sylvester, A. Amar-Zifkin, C. Douglas, B. Morquette, C.S. Moore, A.E. Fournier, microRNA dysregulation in neurodegenerative diseases: a systematic review, Prog. Neurobiol. 182 (2019) 101664, https://doi.org/10.1016/j.pneurobio.2019.101664.
[70] S. Ghafouri-Fard, H. Shoorei, Z. Bahroudi, A. Abak, J. Majidpoor, M. Taheri, An update on the role of miR-124 in the pathogenesis of human disorders, Biomed. Pharmacother. 135 (2021) 111198.
[71] D. Jiang, F. Gong, X. Ge, C. Lv, C. Huang, S. Feng, Z. Zhou, Y. Rong, J. Wang, C. Ji, J. Chen, W. Zhao, J. Fan, W. Liu, W. Cai, Neuron-derived exosomes-transmitted miR-124-3p protect traumatically injured spinal cord by suppressing the activation of neurotoxic microglia and astrocytes, J. Nanobiotechnol. 18 (1) (2020) 105.
[72] C. Ringland, J.E. Schweig, M. Eisenbaum, D. Paris, G. Ait-Ghezala, M. Mullan, F. Crawford, L. Abdullah, C. Bachmeier, MMP9 modulation improves specific neurobehavioral deficits in a mouse model of Alzheimer's disease, BMC Neurosci. 22 (1) (2021) 39, https://doi.org/10.1186/s12868-021-00643-2.
[73] L.K. Hamilton, G. Moquin-Beaudry, C.L. Mangahas, F. Pratesi, M. Aubin, A. Aumont, S.E. Joppé, A. Légiot, A. Vachon, M. Plourde, C. Mounier, M. Tétreault, K.J.L. Fernandes, Stearoyl-CoA Desaturase inhibition reverses immune, synaptic and cognitive impairments in an Alzheimer's disease mouse model, Nat. Commun. 13 (1) (2022) 2061, https://doi.org/10.1038/s41467-022-29506-y.
[74] R. Komori, T. Matsuo, A. Yokota-Nakatsuma, R. Hashimoto, S. Kubo, C. Kozawa, T. Kono, Y. Ishihara, K. Itoh, Regulation of inflammation-related genes through Fosl1 suppression in a levetiracetam-treated pilocarpine-induced status epilepticus mouse model, Int. J. Mol. Sci. 23 (14) (2022) 7608, https://doi.org/10.3390/ijms23147608.
[75] X. Zou, L. Zhong, C. Zhu, H. Zhao, F. Zhao, R. Cui, S. Gao, B. Li, Role of leptin in mood disorder and neurodegenerative disease, Front. Neurosci. 13 (2019) 378, https://doi.org/10.3389/fnins.2019.00378.
[76] M.L. Calió, A.C. Mosini, D.S. Marinho, G.N. Salles, F.H. Massinhani, G.M. Ko, M. A. Porcionatto, Leptin enhances adult neurogenesis and reduces pathological features in a transgenic mouse model of Alzheimer's disease, Neurobiol. Dis. 148 (2021) 105219, https://doi.org/10.1016/j.nbd.2020.105219.
[77] M. Gonzalez-Rodriguez, S. Villar-Conde, V. Astillero-Lopez, P. Villanueva-Anguita, I. Ubeda-Banon, A. Flores-Cuadrado, A. Martinez-Marcos, D. Saiz-Sanchez, Neurodegeneration and astrogliosis in the human CA1 hippocampal subfield are related to hsp90ab1 and bag3 in Alzheimer's disease, Int. J. Mol. Sci. 23 (1) (2021) 165, https://doi.org/10.3390/ijms23010165.
[78] A. Biasi, V. Marino, G. Dal Cortivo, P.E. Maltese, A.M. Modarelli, M. Bertelli, L. Colombo, D. Dell'Orco, A novel GUCA1A variant associated with cone dystrophy alters cGMP signaling in photoreceptors by strongly interacting with and hyperactivating retinal guanylate cyclase, Int. J. Mol. Sci. 22 (19) (2021) 10809, https://doi.org/10.3390/ijms221910809.
[79] D.W. Ethell, L.A. Buhler, Fas ligand-mediated apoptosis in degenerative disorders of the brain, J. Clin. Immunol. 23 (5) (2003) 363–370, https://doi.org/10.1023/a:1025317516396.
[80] M.J. Bullido, A. Martínez-García, M.J. Artiga, J. Aldudo, I. Sastre, P. Gil, F. Coria, D.G. Muñoz, V. Hachinski, A. Frank, F. Valdivieso, A TAP2 genotype associated with Alzheimer's disease in APOE4 carriers, Neurobiol. Aging 28 (4) (2007) 519–523, https://doi.org/10.1016/j.neurobiolaging.2006.02.011.
[81] P.A. Jaeger, K.M. Lucin, M. Britschgi, B. Vardarajan, R.P. Huang, E.D. Kirby, R. Abbey, B.F. Boeve, A.L. Boxer, L.A. Farrer, N. Finch, N.R. Graff-Radford, E. Head, M. Hofree, R. Huang, H. Johns, A. Karydas, D.S. Knopman, A. Loboda, E. Masliah, T. Wyss-Coray, Network-driven plasma proteomics expose molecular changes in the Alzheimer's brain, Mol. Neurodegener. 11 (2016) 31, https://doi.org/10.1186/s13024-016-0095-2.
[82] K.M. Kurkinen, M. Marttinen, L. Turner, T. Natunen, P. Mäkinen, F. Haapalinna, T. Sarajärvi, S. Gabbouj, M. Kurki, J. Paananen, A.M. Koivisto, T. Rauramaa, V. Leinonen, H. Tanila, H. Soininen, F.R. Lucas, A. Haapasalo, M. Hiltunen, SEPT8 modulates β-amyloidogenic processing of APP by affecting the sorting and accumulation of BACE1, J. Cell Sci. 129 (11) (2016) 2224–2238, https://doi.org/10.1242/jcs.185215.
[83] V. Torres, J. Pérez-Montesino, R. Fernández-Santiago, M. Fernández, A. Camara, Y. Compta, M.J. Martí, À. Guerra Beltran, J. Rios, F. Valldeoriola, M. Ezquerra,

DRD4 gene polymorphism and impulse control disorder induced by dopamine agonists in Parkinson's disease, Ann. Clin. Trans. Neurol. 11 (8) (2024) 2222–2229, https://doi.org/10.1002/acn3.52111.
[84] A. Singh, R. Kukreti, L. Saso, S. Kukreti, A. Singh, R. Kukreti, L. Saso, S. Kukreti, Oxidative stress: a key modulator in neurodegenerative diseases, Molecules 24 (8) (2019) 1–20, https://doi.org/10.3390/molecules24081583, 24(8), 1583.
[85] T.L. Hagemann, S.A. Gaeta, M.A. Smith, D.A. Johnson, J.A. Johnson, A. Messing, Gene expression analysis in mice with elevated glial fibrillary acidic protein and Rosenthal fibers reveals a stress response followed by glial activation and neuronal dysfunction, Hum. Mol. Genet. 14 (16) (2005) 2443–2458, https://doi.org/10.1093/hmg/ddi248.
[86] Y. Mi, G. Qi, F. Vitali, Y. Shang, A.C. Raikes, T. Wang, Y. Jin, R.D. Brinton, H. Gu, F. Yin, Loss of fatty acid degradation by astrocytic mitochondria triggers neuroinflammation and neurodegeneration, Nat. Metab. 5 (3) (2023) 445–465, https://doi.org/10.1038/s42255-023-00756-4.
[87] S. Szrok-Jurga, J. Turyn, A. Hebanowska, J. Swierczynski, A. Czumaj, T. Sledzinski, E. Stelmanska, The role of acyl-CoA β-oxidation in brain metabolism and neurodegenerative diseases, Int. J. Mol. Sci. 24 (18) (2023) 13977, https://doi.org/10.3390/ijms241813977.
[88] E. López-Muguruza, C. Matute, Alterations of oligodendrocyte and myelin energy metabolism in multiple sclerosis, Int. J. Mol. Sci. 24 (16) (2023), https://doi.org/10.3390/ijms241612912.
[89] A. Higdon, A.R. Diers, J.Y. Oh, A. Landar, V.M. Darley-Usmar, Cell signalling by reactive lipid species: new concepts and molecular mechanisms, Biochem. J. 442 (3) (2012) 453–464, https://doi.org/10.1042/BJ20111752.
[90] V.E. Kagan, G. Mao, F. Qu, J.P.F. Angeli, S. Doll, C.S. Croix, H.H. Dar, B. Liu, V. A. Tyurin, V.B. Ritov, A.A. Kapralov, A.A. Amoscato, J. Jiang, T. Anthonymuthu, D. Mohammadyani, Q. Yang, B. Proneth, J. Klein-Seetharaman, S. Watkins, H. Bayır, Oxidized arachidonic and adrenic PEs navigate cells to ferroptosis, Nat. Chem. Biol. 13 (1) (2017) 81–90, https://doi.org/10.1038/nchembio.2238.
[91] P.R. Angelova, M.H. Horrocks, D. Klenerman, S. Gandhi, A.Y. Abramov, M. S. Shchepinov, Lipid peroxidation is essential for α-synuclein-induced cell death, J. Neurochem. 133 (4) (2015) 582–589, https://doi.org/10.1111/jnc.13024.
[92] J. Lee, B. Kosaras, S.J. Del Signore, K. Cormier, A. McKee, R.R. Ratan, N. W. Kowall, H. Ryu, Modulation of lipid peroxidation and mitochondrial function improves neuropathology in Huntington's disease mice, Acta Neuropathol. 121 (4) (2011) 487–498, https://doi.org/10.1007/s00401-010-0788-5.
[93] R. Abeti, M.H. Parkinson, I.P. Hargreaves, P.R. Angelova, C. Sandi, M.A. Pook, P. Giunti, A.Y. Abramov, Mitochondrial energy imbalance and lipid peroxidation cause cell death in friedreich's ataxia, Cell Death Dis. 7 (5) (2016) e2237, https://doi.org/10.1038/cddis.2016.111.
[94] E.P. Simpson, Y.K. Henry, J.S. Henkel, R.G. Smith, S.H. Appel, Increased lipid peroxidation in sera of ALS patients: a potential biomarker of disease burden, Neurology 62 (10) (2004) 1758–1765, https://doi.org/10.1212/WNL.62.10.1758.
[95] P.R. Angelova, N. Esteras, A.Y. Abramov, Mitochondria and lipid peroxidation in the mechanism of neurodegeneration: finding ways for prevention, Med. Res. Rev. 41 (2) (2021) 770–784, https://doi.org/10.1002/med.21712.
[96] C. Peña-Bautista, T. Durand, C. Oger, M. Baquero, M. Vento, C. Cháfer-Pericás, Assessment of lipid peroxidation and artificial neural network models in early Alzheimer Disease diagnosis, Clin. Biochem. 72 (2019) 64–70, https://doi.org/10.1016/j.clinbiochem.2019.07.008.
[97] J.A. Barnes-Vélez, F.B. Aksoy Yasar, J. Hu, Myelin lipid metabolism and its role in myelination and myelin maintenance, Innovat. Camb 4 (1) (2023) 100360, https://doi.org/10.1016/j.xinn.2022.100360.
[98] M.C. Kruer, C. Paisán-Ruiz, N. Boddaert, M.Y. Yoon, H. Hama, A. Gregory, A. Malandrini, R.L. Woltjer, A. Munnich, S. Gobin, B.J. Polster, S. Palmeri, S. Edvardson, J. Hardy, H. Houlden, S.J. Hayflick, Defective FA2H leads to a novel form of neurodegeneration with brain iron accumulation (NBIA), Ann. Neurol. 68 (5) (2010) 611–618, https://doi.org/10.1002/ana.22122.
[99] C. Avagliano, L. Coretti, A. Lama, C. Pirozzi, C. De Caro, D. De Biase, L. Turco, M. P. Mollica, O. Paciello, A. Calignano, R. Meli, F. Lembo, G.M. Raso, Dual-hit model of Parkinson's disease: impact of dysbiosis on 6-hydroxydopamine-insulted mice—neuroprotective and anti-inflammatory effects of butyrate, Int. J. Mol. Sci. 23 (12) (2022) 6367, https://doi.org/10.3390/ijms23126367.
[100] Y. Hou, X. Li, C. Liu, M. Zhang, X. Zhang, S. Ge, L. Zhao, Neuroprotective effects of short-chain fatty acids in MPTP induced mice model of Parkinson's disease, Exp. Gerontol. 150 (February) (2021) 111376, https://doi.org/10.1016/j.exger.2021.111376.
[101] Y. Jiang, K. Li, X. Li, L. Xu, Z. Yang, Sodium butyrate ameliorates the impairment of synaptic plasticity by inhibiting the neuroinflammation in 5XFAD mice, Chem. Biol. Interact. 341 (2021) 109452, https://doi.org/10.1016/j.cbi.2021.109452.
[102] M.P. Mollica, G.M. Raso, G. Cavaliere, G. Trinchese, C. De Filippo, S. Aceto, M. Prisco, C. Pirozzi, F. Di Guida, A. Lama, M. Crispino, D. Tronino, P. Di Vaio, R. B. Canani, A. Calignano, R. Meli, Butyrate regulates liver mitochondrial function, efficiency, and dynamics in insulin-resistant obese mice, Diabetes 66 (5) (2017) 1405–1418, https://doi.org/10.2337/db16-0924.
[103] T. Zhao, J. Gu, H. Zhang, Z. Wang, W. Zhang, Y. Zhao, Y. Zheng, W. Zhang, H. Zhou, G. Zhang, Q. Sun, E. Zhou, Z. Liu, Y. Xu, Sodium butyrate-modulated mitochondrial function in high-insulin induced HepG2 cell dysfunction, Oxid. Med. Cell. Longev. 2020 (2020) 1904609, https://doi.org/10.1155/2020/1904609.
[104] D.B.L. Teh, A. Prasad, W. Jiang, Mohd Z. Ariffin, S. Khanna, A. Belorkar, L. Wong, X. Liu, A.H. All, Transcriptome analysis reveals neuroprotective aspects of human reactive astrocytes induced by interleukin 1β, Sci. Rep. 7 (1) (2017) 13988 https://doi.org/10.1038/s41598-017-13174-w.
[105] S. Herman, V. Niemelä, P. Emami Khoonsari, J. Sundblom, J. Burman, A. M. Landtblom, O. Spjuth, D. Nyholm, K. Kultima, Alterations in the tyrosine and phenylalanine pathways revealed by biochemical profiling in cerebrospinal fluid of Huntington's disease subjects, Sci. Rep. 9 (1) (2019) 1–13, https://doi.org/10.1038/s41598-019-40186-5.
[106] M. Kori, B. Aydln, S. Unal, K.Y. Arga, D. Kazan, Metabolic biomarkers and neurodegeneration: a pathway enrichment analysis of alzheimer's disease, Parkinson's disease, and amyotrophic lateral sclerosis, OMICS A J. Integr. Biol. 20 (11) (2016) 645–661, https://doi.org/10.1089/omi.2016.0106.
[107] L. Wang, J. Xia, J. Li, T.L. Hagemann, J.R. Jones, E. Fraenkel, D.A. Weitz, S.-C. Zhang, A. Messing, M.B. Feany, Tissue and cellular rigidity and mechanosensitive signaling activation in Alexander disease, Nat. Commun. 9 (1) (2018) 1899.
[108] J. Swift, I.L. Ivanovska, A. Buxboim, T. Harada, P.C.D.P. Dingal, J. Pinter, J. D. Pajerowski, K.R. Spinler, J.-W. Shin, M. Tewari, F. Rehfeldt, D.W. Speicher, D. E. Discher, Nuclear lamin-A scales with tissue stiffness and enhances matrix-directed differentiation, Science 341 (6149) (2013) 1240104, https://doi.org/10.1126/science.1240104.
[109] S.C. Gammie, A. Messing, M.A. Hill, C.A. Kelm-Nelson, T.L. Hagemann, Large-scale gene expression changes in APP/PSEN1 and GFAP mutation models exhibit high congruence with Alzheimer's disease, PLoS One 19 (1) (2024) e0291995, https://doi.org/10.1371/journal.pone.0291995.
[110] Y. Dong, M. Newman, S.M. Pederson, K. Barthelson, N. Hin, M. Lardelli, Transcriptome analyses of 7-day-old zebrafish larvae possessing a familial Alzheimer's disease-like mutation in psen1 indicate effects on oxidative phosphorylation, ECM and MCM functions, and iron homeostasis, BMC Genom. 22 (1) (2021) 211, https://doi.org/10.1186/s12864-021-07509-1.